

Multigenetic Origin of the X-discontinuity Below Continents: Insights from African Receiver Functions

Stephen Pugh¹, Alistair Boyce^{1,2}, Ian D. Bastow³, C. J. Ebinger⁴, Sanne
Cottaar¹

¹Bullard Laboratories, Department of Earth Sciences, University of Cambridge, UK

²Université Lyon 1, ENS de Lyon, CNRS, UMR 5276 LGL-TPE, F-69622, Villeurbanne, France

³Department of Earth Science and Engineering, Imperial College, London, UK

⁴Department of Earth and Environmental Sciences, Tulane University, New Orleans, LA, USA

Key Points:

- P-to-S converted receiver functions reveal the X-discontinuity beneath the East African Rift System, Morocco, Cameroon, Hoggar and several ocean islands
- Observations are collocated with recent surface magmatism suggesting widely distributed chemical heterogeneity below Africa
- No relationships exist between depth and amplitudes of observed X and estimated temperatures, suggesting multiple causal mechanisms

Corresponding author: Stephen Pugh, sdp43@cam.ac.uk

Abstract

Constraints on chemical heterogeneities in the upper mantle may be derived from studying the seismically observable impedance contrasts that they produce. Away from subduction zones, several causal mechanisms are possible to explain the intermittently observed X-discontinuity (X) at 230–350 km depth: the coesite-stishovite phase transition, the orthorhombic enstatite to high-pressure clinoenstatite phase transition and/or carbonated silicate melting, all of which require a local enrichment of basalt. Africa is host to a broad range of terranes, from Precambrian cores to Cenozoic hotspots with or without lowermost mantle origins. With the absence of subduction below the margins of the African plate for >0.5 Ga, Africa presents an ideal study locale to explore the origins of the X.

Traditional approaches used to map the spatial distribution of horizontal discontinuities observed by receiver functions (RFs), like common conversion-point stacking, ignore the slowness information crucial for discriminating converted upper mantle phases from surface bouncing multiples. By manually assessing depth and slowness stacks for overlapping bins of 1° radius, a normalized vote mapping approach of RF stacks is used to robustly assess the spatial distribution of converted upper mantle phases. The X is mapped beneath Africa between 233 and 340 km depth, revealing patches of heterogeneity proximal to mantle upwellings in Afar, Canaries, Cape Verde, East Africa, Hoggar, and Réunion with further observations beneath Cameroon, Madagascar, and Morocco. There is a lack of an X beneath the whole of southern Africa, and strikingly, the magmatic eastern rift branch of the southern East African Rift. With no relationships existing between depth and amplitudes of observed X and estimated mantle temperatures, multiple causal mechanisms are required across a range of continental geodynamic settings.

Plain Language Summary

Local variations in the mineral chemistry of the upper mantle results in sharp changes in velocity and density. Seismic waves that convert from compressional-to-shear wave propagation (P-to-S) in the upper mantle are sensitive to these jumps in velocity and density, revealing variations in mineral chemistry. One such jump in velocity and density, the X-discontinuity, has several proposed explanations and detecting its presence across a range of mantle conditions allows us to test these possible hypotheses.

48 We search for observations of the X-discontinuity, where P-to-S conversion occurs
49 between 230–350 km depth, beneath the continent of Africa. Our observations are found
50 beneath many regions of surface magmatism across Africa, suggesting that the X-discontinuity
51 has multiple origins.

52 **1 Introduction**

53 **1.1 Overview**

54 Mineral phase transitions cause abrupt jumps in local velocity and density struc-
55 ture of the mantle. The seismically observable impedance contrasts resulting from these
56 transitions are termed seismic discontinuities. Due to estimated pressure-temperature
57 dependence of discontinuity depth, the uplift or depression of some global seismic dis-
58 continuities can be studied as a thermometer for local mantle structure (e.g., Helffrich,
59 2000, 2002). On the other hand, non-global, localized seismic discontinuities can map
60 the local enrichment of chemical heterogeneity, such that the impedance contrast of the
61 seismic discontinuity renders it seismically observable. One such non-global discontinu-
62 ity at 230–350 km depth is the X-discontinuity (X; e.g., Revenaugh & Jordan, 1991; Deuss
63 & Woodhouse, 2004; Schmerr, 2015) that may be used as a tracer for upper mantle chem-
64 ical heterogeneity, the distribution of which may shed important insights into mantle dy-
65 namics and the extent of chemical equilibration.

66 Prior observations of the X-discontinuity have been concentrated in the oceans (Deuss
67 & Woodhouse, 2002; Schmerr et al., 2013; Schmerr, 2015; Pugh et al., 2021). While ob-
68 servations of the X at subduction zones are thought to track hydration reactions (Revenaugh
69 & Jordan, 1991) and eclogite (Schmerr et al., 2013) in downgoing plates, importantly,
70 observations of the X above mantle plumes may inform us about both the distribution
71 of chemical heterogeneity in the lower mantle and its subsequent transportation to the
72 upper mantle (e.g. C. D. Williams et al., 2019; Pugh et al., 2021). In regions of elevated
73 mantle temperatures, several causal mechanisms have been proposed to explain obser-
74 vations of the X including the coesite-stishovite (Co-St) phase transition (Q. Williams
75 & Revenaugh, 2005), orthorhombic enstatite to high-pressure clinoenstatite pyroxene (OEN-
76 HCEN) phase transition (Woodland, 1998) and the deep formation of partial melts (e.g.,
77 Dasgupta et al., 2013). For further discussion of causes of the X-discontinuity away from
78 elevated temperatures see Schmerr (2015), Kemp et al. (2019) and Pugh et al. (2021).

79 In contrast to the oceans, studies of the X-discontinuity in continental hotspot set-
 80 tings have received comparatively little attention (e.g., Rein et al., 2020), due to sam-
 81 pling deficiencies in reflected phase studies (e.g., Schmerr, 2015) and the distribution of
 82 overlying stations required for converted phase studies. Africa presents the perfect study
 83 locale to search for the X because it is host to widely distributed Cenozoic magmatism
 84 (e.g., Ebinger & Sleep, 1998; Furman et al., 2006; Pik et al., 2006; de Gouveia et al., 2018),
 85 with debated thermochemical nature, origin/scale depth (e.g., Simmons et al., 2007; Civiero
 86 et al., 2015; Boyce et al., 2021) and geodynamic causal mechanism (Fairhead & Binks,
 87 1991; Ebinger & Sleep, 1998; King & Anderson, 1998; King & Ritsema, 2000; Gallacher
 88 & Bastow, 2012; Milelli et al., 2012). For example, Boyce et al. (2021) propose that a
 89 hot, chemically distinct upwelling beneath the southern East African Rift System (EARS;
 90 Figure 1b) is sourced from the African LLVP, while magmatism in Ethiopia may lie above
 91 an additional purely thermal upwelling whose depth extent is uncertain. Elsewhere, smaller
 92 volume magmatism along the Cameroon Volcanic Line (CVL; Figure 1b) in west Africa
 93 lacks the age progression associated with a classic mantle plume (Montigny et al., 2004),
 94 and has been explained instead by several alternative mechanisms: shear zone reactiva-
 95 tion, small-scale convection, and lithospheric delamination (e.g., Fairhead & Binks, 1991;
 96 King & Ritsema, 2000; Reusch et al., 2010, 2011; Gallacher & Bastow, 2012; Milelli et
 97 al., 2012; De Plaen et al., 2014).

98 Previous observations of the X beneath Africa have been limited to a few widely
 99 scattered SS precursor observations (Deuss & Woodhouse, 2002) and localized scatter-
 100 ers in regional $P'P'_{df}$ precursors studies (Xu et al., 1998) and P-to-S receiver functions
 101 (RFs) (Owens et al., 2000; Rein et al., 2020; Pugh et al., 2021). Such point observations
 102 do not span competing models of hotspot tectonism, limiting their ability to interrogate
 103 the causal mechanisms of the X in the upper mantle. A detailed, continent-wide study
 104 of the X is required to understand its exact geographical distribution and the mechanisms
 105 that lead to observation. Using seismic network data that sit atop sites of African man-
 106 tle upwellings, Cenozoic magmatism, and cratonic lithosphere, we map the presence of
 107 the X-discontinuity beneath the African continent using receiver functions.

108 **1.2 African Cenozoic Magmatism**

109 Cenozoic magmatism across the African continent has been linked to multiple man-
 110 tle upwellings of varying scale, geodynamic causal mechanism and thermochemical na-

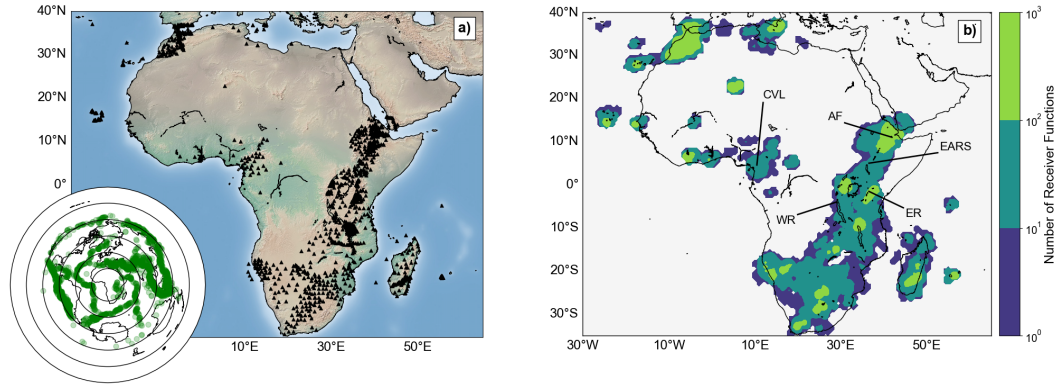


Figure 1. a) Station distribution (black triangles) across Africa and its surrounding islands. The inset globe shows the earthquake distribution (green circles) for this study and black circles represent distance intervals of 30° at $30\text{--}180^\circ$ epicentral distance from the centre of Africa. b) Receiver function distribution across Africa for piercepoints of P300s at 300 km depth using raypaths through PREM (Dziewonski & Anderson, 1981) calculated using the TauP toolkit (Crotwell et al., 1999). AF: Afar, CVL: Cameroon Volcanic Line, EARS: East African Rift System, ER: Eastern Rift, WR: Western Rift.

111 ture. Uplifted plateaux in northeast, central and southern Africa (Lithgow-Bertelloni &
 112 Silver, 1998) and the 45 Ma Ethiopian flood basalts (e.g., Furman et al., 2006; Rooney,
 113 2017) have been associated with ongoing rift-related magmatism along the EARS. One
 114 or more mantle upwellings have been invoked to explain uplift, elevated $^3\text{He}/^4\text{He}$ anom-
 115 alies, the surface distribution of magmatism, and the observed mantle transition zone struc-
 116 ture (Ebinger & Sleep, 1998; Furman et al., 2006; Pik et al., 2006; Rooney, 2017; de Gou-
 117 veia et al., 2018; Chang et al., 2020; Boyce & Cottaar, 2021). Global tomographic mod-
 118 els reveal a broad, low-wavespeed anomaly extending from the core-mantle boundary be-
 119 neath southern Africa to the surface below the EARS (Ritsema et al., 1999, 2010; Chang
 120 et al., 2015; French & Romanowicz, 2015). Some continental to regional scale models de-
 121 compose this broad anomaly into multiple smaller low-wavespeed anomalies in East Africa
 122 linked to mantle plume activity (Emry et al., 2019; Chang et al., 2020; Boyce et al., 2021).
 123 However, the exact number of upwellings is debated with up to three being proposed to
 124 explain surface magmatism (Chang et al., 2020) and further suggestions that these could
 125 comprise multiple smaller-scale upwellings in the upper mantle (Furman et al., 2006; I. Bas-
 126 tow et al., 2008; Civiero et al., 2015, 2016).

127 The linear trend of Cenozoic magmatism across Morocco has previously been at-
128 tributed to edge-driven convection (King & Anderson, 1998; King & Ritsema, 2000; Mis-
129 senard & Cadoux, 2011; Kaislaniemi & van Hunen, 2014), delamination of the root of
130 the Atlas mountains (Bezada et al., 2014) and diversion of the Canarian mantle plume
131 (Duggen et al., 2009; Mériaux et al., 2015; Miller et al., 2015). Whilst several tomographic
132 models suggest the Canaries sit atop a whole mantle plume (French & Romanowicz, 2015;
133 Marignier et al., 2020), geochemical evidence suggests that Moroccan and Canarian mag-
134 matism do not share a single deep origin and are attributable to several upper mantle
135 upwellings (Lustrino & Wilson, 2007; van den Bogaard, 2013). However, recent tomo-
136 graphic models show these upper mantle upwellings are connected at depth (Civiero et
137 al., 2018), with upwelling beneath the Azores and Cape Verde also connected to the same
138 common deep source (Saki et al., 2015).

139 The CVL in west Africa is a linear chain of volcanoes oriented NE/SW including
140 four islands offshore in the Gulf of Guinea (Fitton, 1980; Déruelle et al., 1991). Despite
141 being observed in at least one global tomographic model (e.g., French & Romanowicz,
142 2015), the robustness of a whole mantle plume beneath Cameroon in tomographic mod-
143 els is debated (Emry et al., 2019; Marignier et al., 2020; Boyce et al., 2021). With no
144 age progression to magmatism along the CVL (Montigny et al., 2004), several alterna-
145 tive mechanisms have been invoked to explain magmatism including edge-driven con-
146 vection (King & Anderson, 1998; King & Ritsema, 2000; Reusch et al., 2010, 2011), litho-
147 spheric delamination and/or fault zone reactivation (e.g., Milelli et al., 2012; De Plaen
148 et al., 2014; Fairhead & Binks, 1991; Gallacher & Bastow, 2012), and lateral flow of plume
149 material from East Africa (Ebinger & Sleep, 1998).

150 In central Madagascar, magmatism has been linked with uplift, lithospheric thin-
151 ning and intercontinental extension (Melluso et al., 2016; Cucciniello et al., 2017). An
152 alternative view connects central Madagascan magmatism to lateral flow of plume ma-
153 terial from East Africa as suggested beneath Comoros and northern Madagascar (Ebinger
154 & Sleep, 1998). Recent seismological studies find a thin mantle transition zone (MTZ)
155 beneath south and central Madagascar (Boyce & Cottaar, 2021) and low wavespeed anoma-
156 lies extending to the lower mantle (Boyce et al., 2021; Tsekhmistrenko et al., 2021), sug-
157 gesting the presence of a thermal upwelling in this region. In nearby Réunion, magma-
158 tism has been shown to be underlain by a mantle plume from seismic tomography (French

159 & Romanowicz, 2015; Tsekhmistrenko et al., 2021) and anomalously high $^3\text{He}/^4\text{He}$ ra-
160 tios (Graham et al., 1990).

161 **2 Data and Method**

162 **2.1 Data**

163 We extend the receiver function (RF) data sets of Boyce and Cottaar (2021) and
164 Pugh et al. (2021) using data recorded up until October 2021 downloaded from the In-
165 corporated Research Institutions for Seismology (IRIS) Data Management System for
166 teleseismic earthquakes with magnitude (M_W) ≥ 5.5 at epicentral distances of 40-90°.
167 We capitalize on the new TRAILS data set in the Turkana Depression (I. D. Bastow, 2019;
168 Ebinger, 2018; Kounoudis et al., 2021), and a further data set in northeast Uganda (Nyblade,
169 2017) where there is a paucity of station coverage in our RF data set along the East African
170 Rift (EAR). This results in $\sim 200,000$ event-station pairs recorded between January 1990
171 and October 2021, recorded at $>1,800$ stations. The distribution of stations and events
172 is displayed in Figure 1a and a full list of networks used in this study can be found in
173 the Open Research Section and Table S1.

174 **2.2 Receiver Functions**

175 We use P wave RFs to highlight P to S converted phases (Pds; where d denotes
176 the depth of conversion) from the upper mantle. Pds converted from the X are herein
177 referred to as PXs. SV waves converted from an incident P wave are radially polarized.
178 RF analysis (Langston, 1979) constitutes deconvolution of the vertical component seis-
179 mogram from the radial component assuming that the vertical component represents a
180 convolution of the earthquake source, instrument response and some noise. Subsequently
181 the RFs can be stacked to emphasize the low-amplitude Pds arrivals. RFs record the dis-
182 continuity structure at depth near a seismometer. We use the iterative, time-domain de-
183 convolution method (Ligorria & Ammon, 1999) to construct RFs, which iteratively adds
184 Gaussian pulses to reduce the least squares misfit between the predicted and observed
185 radial seismograms. Traces are windowed 25s before and 150s after the P-wave to in-
186 clude depth phases in the source deconvolution and remove correlated noise between the
187 vertical and radial traces. Data are bandpass filtered with corner frequencies 0.01 and
188 0.4 Hz, isolating the frequency band with the largest X amplitudes (Pugh et al., 2021).

189 Approximately 10% of RFs remain after automatic quality control (see Pugh et al.,
 190 2021, for details), leaving 20,630 RFs. Of these, 18,017 remain after further manual in-
 191 spection to remove obvious low quality RFs (Section S3 and Figure S1a).

192 RF are initially converted from time-to-depth using the 1D velocity model PREM
 193 (Dziewonski & Anderson, 1981). However, 1D time-to-depth conversions can result in
 194 >20 km of error on upper mantle discontinuities (Pugh et al., 2021). To perform 3D ve-
 195 locity corrections SEMUCB.WM1 (French & Romanowicz, 2014), and a recent model
 196 of the African continent, AF2019 (Celli, Lebedev, Schaeffer, & Gaina, 2020), are used.
 197 While tomographic models suffer from sparse and uneven data coverage beneath Africa,
 198 the resolution should be greatest where receiver functions are located. This condition
 199 is valid especially for the recent model of Celli, Lebedev, Schaeffer, and Gaina (2020),
 200 which incorporates body waves from recently available seismic arrays.

201 **2.3 Stacking and Vote Mapping**

202 The amplitudes of Pds on individual RFs are <10% of the incoming P wave and
 203 will typically be lower than the noise on an individual trace. As such, high-quality RFs
 204 with overlapping sensitivity in upper mantle are stacked to amplify coherent Pds and
 205 suppress noise. Following the spiral distribution of Rakhmanov et al. (1994), equidistant
 206 bins of radius 111 km ($\sim 1^\circ$ at the equator) are defined across the globe overlapping by
 207 $\sim 0.5^\circ$. All RFs that traverse the upper mantle within a bin, estimated using their ray
 208 theoretical pierce point at 300 km depth from the TauP toolkit (Crotwell et al., 1999),
 209 are stacked together in the depth and time-slowness domains (see Pugh et al., 2021, for
 210 details). Visual inspection shows that the majority of stacks with <30 RFs are of poor
 211 quality. Therefore, stacks containing >30 RFs are assessed by the visibility of Pds phases
 212 in slowness stacks as outlined in Pugh et al. (2021) to determine robust (Figure 2a and
 213 b), potential (Figure 2c and d) and null (Figure 2e and f) observations of the X-discontinuity.

214 Common conversion point stacking (Dueker & Sheehan, 1997) has previously been
 215 used to map the 410 km and 660 km discontinuities across Africa, as well as the presence
 216 of mid-mantle discontinuities (Thompson et al., 2015; Reed et al., 2016; Boyce & Cot-
 217 taar, 2021). This technique relies on stacking all depth converted RFs that traverse the
 218 upper mantle within a defined Fresnel zone width at each point in a regular grid. Whilst
 219 this provides a powerful tool for analyzing these surfaces, slowness information is not con-

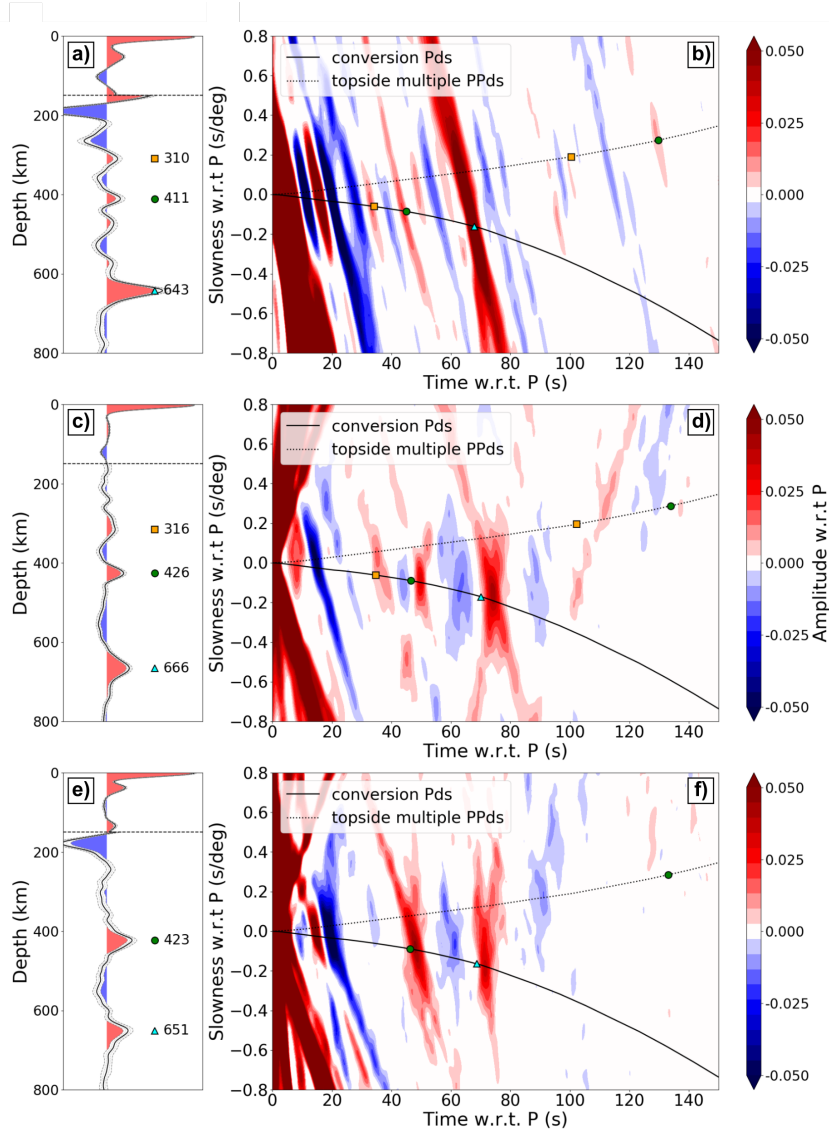


Figure 2. Example stacks for X-discontinuity classifications of Robust (a and b), Potential (c and d) and Null (e and f) respectively. Depth (a, c and e) and slowness stacks (b, d and f) with 130, 370 and 137 RFs, filtered at 0.01–0.4 Hz. Depth stacks (a, c and e): Time-to-depth converted RFs are linearly stacked with the black line marking amplitude (normalized to P) and dashed lines marking $2\sigma_M$. Amplitudes are multiplied by 5 below the horizontal dashed line at 150 km depth. Stacks are converted from time-to-depth using SEMUCB_WM1. Colored symbols mark significant peaks from PXs (orange squares), P410s (green circles), and P660s (cyan triangles). Slowness stacks (b, d and f): RFs with amplitude $>2\sigma_M$ normalized to P stacked in the time-slowness domain. Predicted time-slowness curves are shown for the direct (Pds) and multiple (PPvds) phases. The colored symbols correspond to predicted times and slownesses for direct arrivals and PPvds multiples for significant arrivals in the depth stacks computed from PREM.

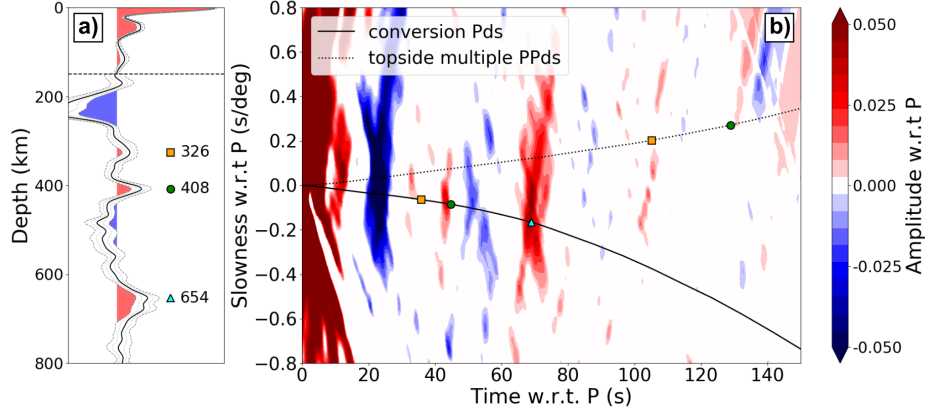


Figure 3. Example of a contaminating PPvds multiple. Depth (a) and slowness stack (b) for 31 RF, filtered at 0.01–0.4 Hz. Depth stack: Time-to-depth converted RFs are linearly stacked with the black line marking amplitude (normalized to P) and dashed lines marking $2\sigma_M$. Amplitudes are multiplied by 5 below the horizontal dashed line at 150 km depth. The stack is converted from time-to-depth using SEMUCB-WM1. Colored symbols mark significant peaks from PXs (orange squares), P410s (green circles), and P660s (cyan triangles). Slowness stack: RFs with amplitude $>2\sigma_M$ normalized to P stacked in the time-slowness domain. Predicted time-slowness curves are shown for the direct (Pds) and multiple (PPvds) phases. The colored symbols correspond to predicted times and slownesses for direct arrivals and PPvds multiples for significant arrivals in the depth stacks computed from PREM.

220 considered. With the presence of shallow upper mantle PPvds phases contaminating the depth
 221 and slowness interval considered for the X (e.g., Figure 3), common conversion point stack-
 222 ing is deemed unsuitable.

223 Here, a vote mapping procedure (e.g., Lekic et al., 2012) is carried out whereby each
 224 bin that intersects a $0.5^\circ \times 0.5^\circ$ region counts a “vote” towards that region, with robust,
 225 potential and null bins voting +1, 0, or -1 to that region respectively. Regions with ≥ 2
 226 votes in Figure 4 are normalized by the number of votes to account for a heterogeneous
 227 data coverage. Regions with < 2 votes are masked. We interpret the resulting smooth
 228 map as an increasing likelihood that an X is present (positive values) or not present (neg-
 229 ative values). Using this approach of a vote map with overlapping bins reduces the de-
 230 pendence of our results on a specific choice of grid. Whilst the depth information of com-
 231 mon conversion point stacking is lost, this provides a robust representation of the dis-

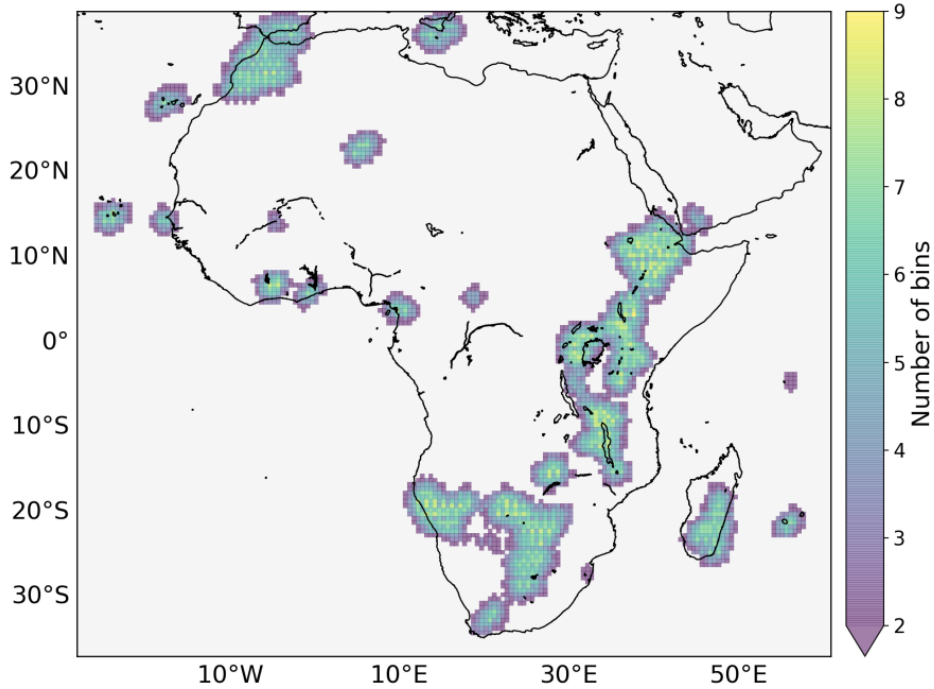


Figure 4. Number of 1° radius bins intersecting each $0.5^\circ \times 0.5^\circ$ bin for normalized vote mapping.

232 tribution of the X and its potential length scales across the continent including depth
 233 and slowness information.

234 **3 Results**

235 **3.1 Geographical distribution of the X-discontinuity**

236 The upper mantle beneath the African continent is imaged using >18,000 RFs. Depth
 237 and slowness stacks are computed to identify observations of the X for nearly 600 over-
 238 lapping bins of 1° radius. Using a normalized vote mapping approach in Figure 5, the
 239 geographical distribution and length-scales of the X-discontinuity are displayed across
 240 the African continent. X observations cluster around the Canaries, Cameroon, Cape Verde,
 241 Ethiopia, the Hoggar volcanic province, southernmost Madagascar, Morocco, and Re-
 242 union with intermittent observations appearing along the Western Rift (WR). Null ob-
 243 servations are prevalent in southern Africa, along the Eastern Rift (ER), and in north-

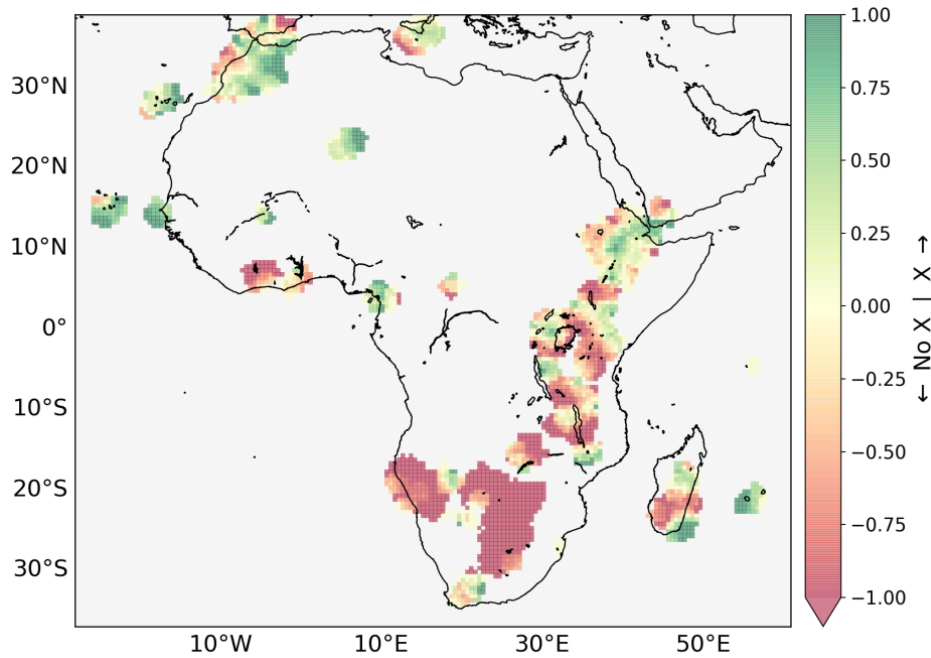


Figure 5. Normalized vote map of X-discontinuity observations for 597 overlapping 1° radius bins with ≥ 2 votes on a $0.5^\circ \times 0.5^\circ$ grid with darkening green colours showing an increasing likelihood of the X and darkening red colours showing an increasing likelihood of no X. Votes are based upon the presence of the X-discontinuity in slowness stacks.

ern Madagascar. This distribution is explored further in the context of magmatism in
 244 Section 4.2.
 245

The number of RFs in a stack has little bearing on its classification (Figure S2).
 246 However, the backazimuth distribution of RFs has a strong control on epicentral distance
 247 distribution, thus determining the streakiness of slowness stacks and potentially mask-
 248 ing X observations (Figure S4; Section S4).
 249

3.2 Depth distribution of the X-discontinuity

Nearly 600 depth and slowness stacks with > 30 RFs are visually inspected for the
 251 presence of the X-discontinuity. Upper mantle positive conversions are present in the depth
 252 range of 212–377 km, 233–340 km, and 235–347 km depth for 262 stacks using PREM,
 253 SEMUCB_WM1 and AF2019, respectively. Using the criteria set out in Pugh et al. (2021),
 254 172 stacks are classed as robust with the correct slowness for PXs, 121 stacks are classed
 255

256 as potential, 303 stacks are classed as null and only one stack is classed as poor qual-
 257 ity; 59 stacks contain robust observations of PPvXs.

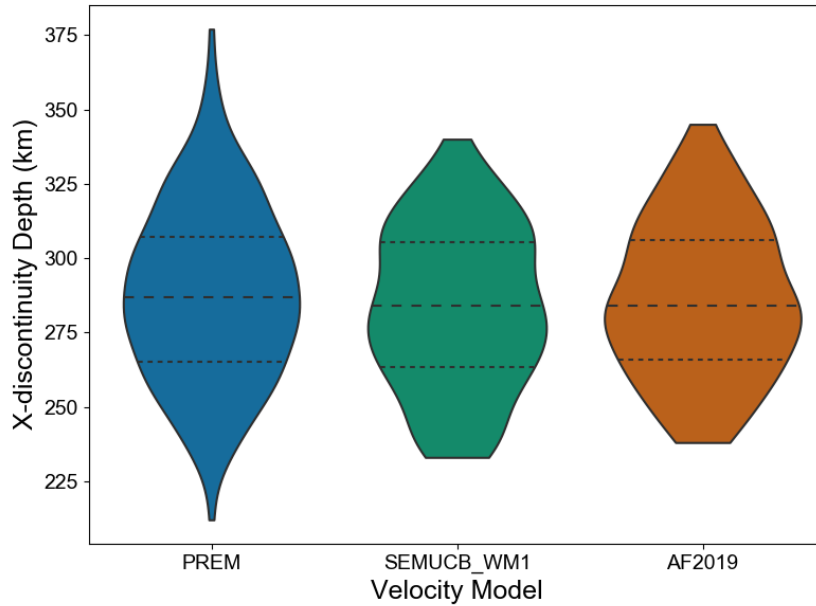


Figure 6. Violin plots of X-discontinuity depths observed in depth stacks cut to the minimum and maximum observations for the three velocity models used in this study: PREM, SEMUCB_WM1 and AF2019. Dashed lines mark the 1st, 2nd and 3rd quartiles of each violin.

258 Including slowness information, robust X-discontinuity depths range between 233
 259 and 340 km, centered around a mean depth of 284 km with lower and upper quartiles of
 260 264 and 305 km respectively for SEMUCB_WM1 (Figure 6). Though the total data dis-
 261 tribution shifts deeper when using AF2019 (238-345 km depth), the mean depth and quar-
 262 tiles (284 km, 266 km and 306 km) are remarkably similar to those from SEMUCB_WM1.

263 SEMUCB_WM1 is preferred for depth correction as temperature variation and to-
 264 pography calculated in Section S5 suggest it better accounts for upper mantle velocity
 265 structure. Subsequently, depths reported below are as converted using SEMUCB_WM1
 266 and displayed in Figure 7.

267 Only 34% of the depth and slowness stacks that contain PXs also contain PPvXs
 268 arrivals. It is logical that the percentage of stacks containing PPvXs is lower beneath
 269 the continents than the 60% percent in Pugh et al. (2021), where stacks are predomi-
 270 nantly made beneath ocean islands. The heterogeneous nature of the continental crust

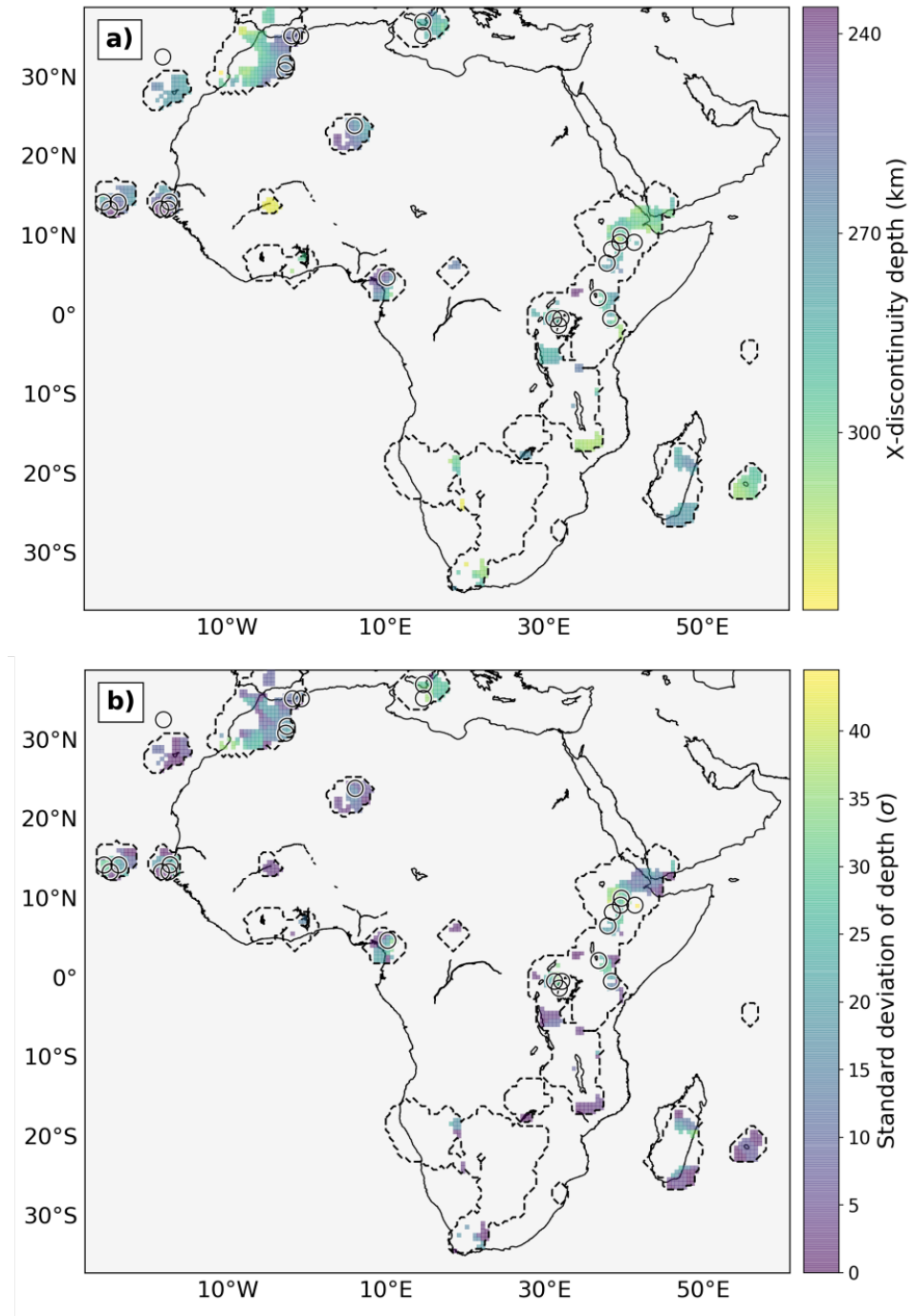


Figure 7. Vote maps of a) X depth and b) standard deviation of depths (σ) for 597 overlapping 1° radius bins with ≥ 2 votes, and an average vote ≥ 0.25 (Figure 5), on a $0.5^\circ \times 0.5^\circ$ grid. Black circles mark bins where two X observations are made and black dashed contours mark the enter of the vote map (Figures 4 and 5).

271 and lithosphere may inhibit coherent stacking of PPvXs, especially considering the greater/variable
272 thickness of the continental lithosphere.

273 4 Discussion

274 4.1 Potential trends in the X-discontinuity

275 We explored discontinuities in the upper mantle beneath the African continent and
276 surrounding ocean islands in ~ 600 equally spaced depth and slowness stacks (Figure 8).
277 Scattered observations of the X exist in nearly 30% of the stacks over a broad depth range
278 of 233–340 km. Figure 8a shows that the depth and amplitude distribution of these re-
279 sults is comparable to those in Pugh et al. (2021) with the largest amplitudes of $\geq 8\%$
280 of the main P wave arrival found at ~ 280 km depth and smaller amplitudes of $\leq 3\%$ be-
281 low 330 km depth. No clear correlation exists between the depth of the X and its am-
282 plitude (Figure 8a). We calculate average upper mantle temperatures at 200–400 km depth
283 for every stack at $\pm 1^\circ$ latitude and longitude using the temperature deviations found
284 in the geophysical-petrological inversion of Fullea et al. (2021). No correlation can be
285 found between the depth of the observed X and these local thermal perturbations (Fig-
286 ure 8b) and the X is no more readily observed at elevated upper mantle temperatures
287 than at depressed temperatures (Figure S6). However, null observations of the X are more
288 readily found at depressed mantle temperatures (Figure S6). Without a trend in the temperature-
289 depth space, it is impossible to infer a Clapeyron slope for the X. With no Clapeyron
290 slope, and such a broad range in depths and amplitudes, we conclude multiple causal mech-
291 anisms are responsible for the X below continents.

292 X discontinuity observations are broadly found beneath the thinnest lithosphere
293 across the African continent (Figure S7) using three global tomographic models (Schaeffer
294 & Lebedev, 2013; Debayle et al., 2016; Priestley et al., 2018). X observations closely track
295 the thin lithosphere of the Main Ethiopian Rift and are present beneath several ocean
296 islands. However, the X is absent beneath thick cratonic lithosphere. One explanation
297 for the lack of X observations below thick lithosphere concerns multiples. PPvds mul-
298 tiple are expected to arrive at seismic stations at the same time as PXs conversions when
299 $d \approx 80\text{--}100$ km, similar to the depth of the mid-lithospheric discontinuities reported in
300 S wave RF studies beneath the Tanzanian (Wölbern et al., 2012) and Kalahari (Sodoudi
301 et al., 2013) cratons, though these discontinuities are observed with the opposite polar-

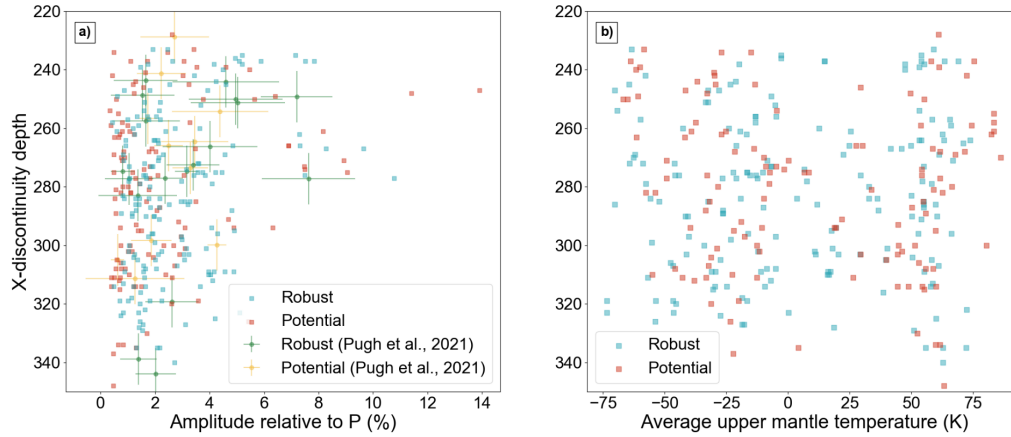


Figure 8. a) Depth and amplitude distribution of 172 robust X-discontinuity observations, and 121 potential X-discontinuity observations plotted alongside the observations of Pugh et al. (2021). Depths are converted using SEMUCB-WM1. Error bars are calculated in depth and amplitude using 10 jackknife resamples with 90% of the data in each sample. Amplitude error bars represent $\pm 2 \sigma_M$ of the mean of each stack whereas depth error bars represent the mean width of the PXs $+2 \sigma_M$ peak at the PXs amplitude across all stacks. Error bars are not displayed for observations from this study to avoid overcrowding the axes. b) Depth and average upper mantle temperature distribution of 172 robust X-discontinuity observations, and 121 potential X-discontinuity observations. Temperatures deviations are taken from Fullea et al. (2021) and averaged at 200–400 km depth.

ity to the X. As for the lithosphere-asthenosphere boundary, only 13–21% of $0.5^\circ \times 0.5^\circ$ bins in our vote map sample lithosphere between 80 and 100 km thick according to maps derived by Hoggard et al. (2020) using velocity models SLNAAFSA (Schaeffer & Lebedev, 2013, 2014; Celli, Lebedev, Schaeffer, & Gaina, 2020; Celli, Lebedev, Schaeffer, Ravenna, & Gaina, 2020), CAM2016 (Ho et al., 2016; Priestley et al., 2018) and 3D2015-sv (Debayle et al., 2016). As such, interfering phases are unlikely to be a persistent issue for RF stacks. While thick heterogeneous lithosphere could result in the incoherent stacking of RFs, very low standard error in null stacks beneath cratons suggests that, for the thickest lithosphere, this does not occur.

In line with our correlation between null observations and depressed upper mantle temperatures, we suggest a cooler asthenospheric mantle underlying thicker lithosphere may present unfavorable conditions of X formation/visibility. This is, however, challeng-

314 ing to prove with our results alone. For stacks classed as potential, limited backazimuth
315 and epicentral distance distribution resulting in streaky slowness stacks seems to have
316 the largest control on the X observation robustness (Section S4).

317 While no quantitative relationship is found between the depth of the observed X
318 and estimated temperatures in the upper mantle, most regions of Quaternary-recent mag-
319 matism are associated with an X observation: they are located proximally to several ocean
320 islands (Canaries, Cape Verde, Réunion), Morocco, Cameroon, the East Africa Rift and
321 Madagascar, and overlap with our previous RF stacks (Pugh et al., 2021). While robust
322 X observations were found in the Canaries and Cameroon in Pugh et al. (2021), this cur-
323 rent study highlights the importance of studying the X over short wavelengths with po-
324 tential observations in Cape Verde, Hoggar, Afar and Réunion now found to be robust.
325 The non-robustness of X signals in these regions in Pugh et al. (2021) may have been
326 the result of unimodal backazimuth and epicentral distance distributions causing streaky
327 slowness stacks (e.g., Figure S4) or topography across the X on short wavelengths as can
328 be seen for Cape Verde, Hoggar and Réunion (Figure 7). These locations all host Qua-
329 ternary volcanoes and/or Cenozoic magmatism (Figure 9). Alongside X observations in
330 regions of ongoing subduction (e.g., Revenaugh & Jordan, 1991; Schmerr et al., 2013),
331 these observations suggest the X to be related to recent upwelling or downwelling, with
332 chemical heterogeneity mixed into the mantle during subsequent mantle convection. The
333 causal mechanisms and implications of these observations are discussed below to explore
334 the cause of the X-discontinuity across upwellings of variable geodynamic origin.

335 **4.2 Links to Surface and Geodynamic Features**

336 **4.2.1 East Africa**

337 The presence of the X beneath East Africa may be related to chemical heterogene-
338 ity introduced by mantle upwellings in the region (Simmons et al., 2007; Rooney, 2017;
339 Boyce & Cottaar, 2021). Robust X observations underlie several sections of the EARS
340 from Afar in the north, through Ethiopia and two patches beneath the WR, to a small
341 patch in Mozambique at depths of 270-320 km (Figure 10a). Notable null results are seen
342 beneath the Turkana Depression, along the ER, and under the Tanzanian craton where
343 substantial volumes of data exist. In Ethiopia, X depths gradually increase northwards
344 to Afar (Figure 11). If the X is controlled by a common causal mechanism beneath the

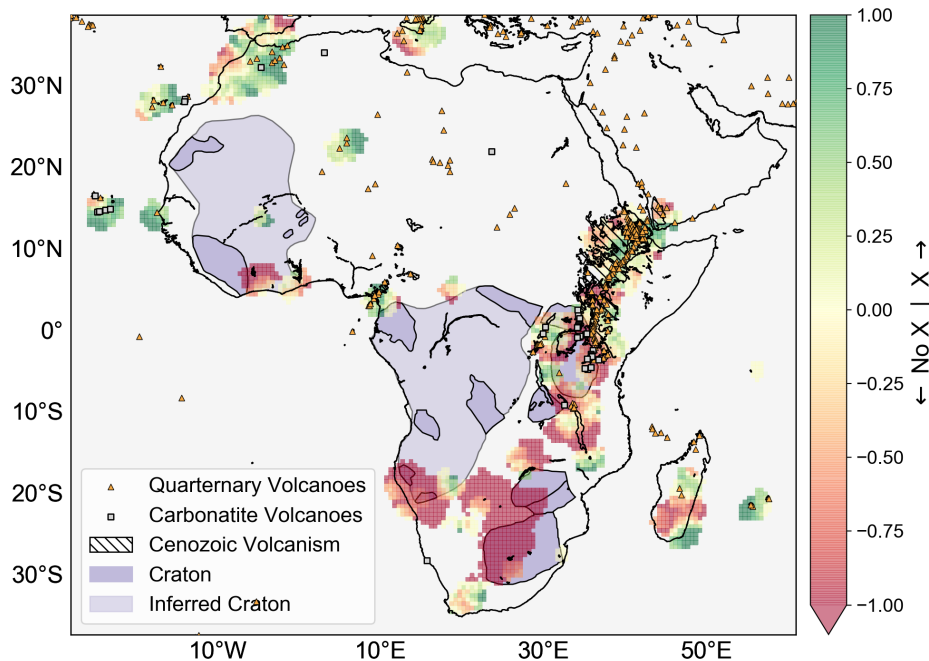


Figure 9. X-discontinuity vote map (Figure 5) plotted above cratons and Cenozoic magmatism adapted from (Begg et al., 2009; Boyce et al., 2021; Kounoudis et al., 2021). Carbonatite volcanoes plotted are ~ 45 Ma-recent (Woolley & Kjarsgaard, 2008; Muirhead et al., 2020).

345 EARS, the positive Clapeyron slope of the Co-St (Akaogi et al., 2011) would suggest an
 346 increase in temperature towards Afar, consistent with reductions in seismic wavespeed
 347 (Boyce et al., 2021). However, the impact of the variable presence of melt on seismic wavespeeds
 348 makes isolating thermal controls on seismic heterogeneity difficult to isolate (e.g., Rooney
 349 et al., 2012; I. Bastow et al., 2008).

350 There is significant debate as to the number of plumes that exist in the upper man-
 351 tle in East Africa and whether they are commonly or uniquely sourced. One to three whole-
 352 mantle plumes of variable thermochemical nature or multiple upper mantle plume heads
 353 have been proposed to explain surface magmatism on the strength of seismological and
 354 geochemical evidence (Ebinger & Sleep, 1998; Furman et al., 2006; Pik et al., 2006; Civiero
 355 et al., 2015, 2016; de Gouveia et al., 2018; Chang et al., 2020; Boyce & Cottaar, 2021).
 356 Robust X observations closely follow the Main Ethiopian Rift from Afar to southern Ethiopia,
 357 and reappear along parts of the western rift marked by Quaternary volcanism (Figures

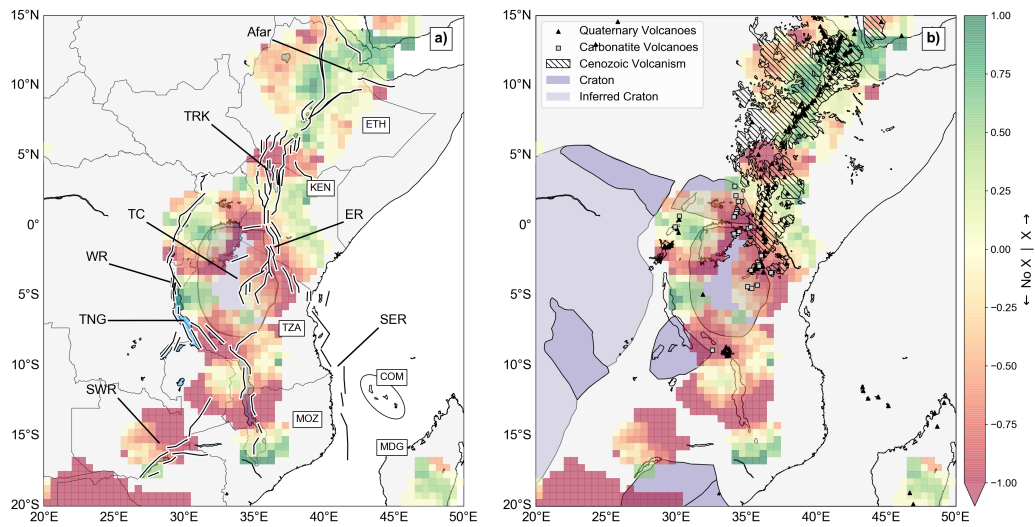


Figure 10. a) X-discontinuity vote map (Figure 5) plotted above the Tanzanian Craton (TC - purple) and lakes (blue) along the EARS (TRK, Lake Turkana; TNG, Lake Tanganyika). Major faults adapted from Jones (2020) are marked with thick black and white lines and reveal the Eastern, Western, Southeastern and Southwestern rifts (ER, WR, SER, SWR). National borders are marked with thin black lines and countries referred to in text are labelled (COM, Comoros Archipelago including Mayotte; ETH, Ethiopia; KEN, Kenya; MDG, Madagascar; MOZ, Mozambique; TZA, Tanzania). b) X-discontinuity vote map (Figure 5) plotted above cratons and Cenozoic magmatism adapted from (Begg et al., 2009; Boyce et al., 2021; Kounoudis et al., 2021). Carbonatite volcanoes plotted are ~ 45 Ma-recent (Woolley & Kjarsgaard, 2008; Muirhead et al., 2020).

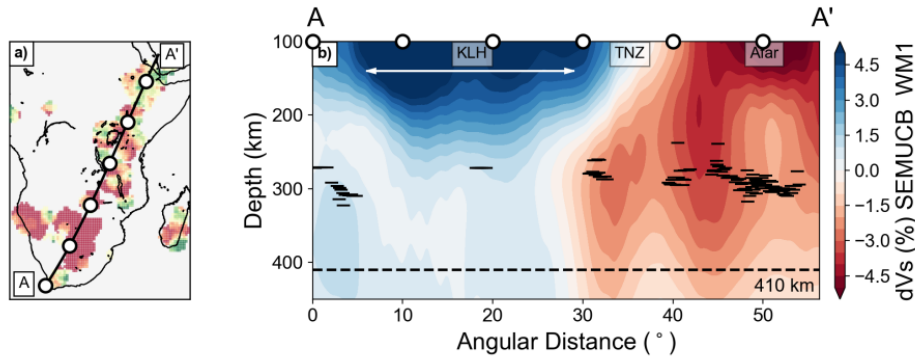


Figure 11. Along profile a), a cross-section b) of X-discontinuity depths of robust observations from South Africa to Afar plotted above the tomographic model SEMUCB.WM1 (French & Romanowicz, 2015). X-discontinuity depths are taken from bins in Figure 7 ≤ 250 km from the line of section. KLH, Kalahari Craton; TNZ, Tanzanian Craton. The white arrow marks the horizontal extent of the Kalahari Craton.

358 10). Widely distributed X observations suggest chemical heterogeneity is pervasive through-
 359 out East Africa around 300 km depth and so presents no clear support for multiple small
 360 scale upwellings that have been reported by some workers (Civiero et al., 2015, 2016) or
 361 underlying plumes of variable thermochemical nature (Boyce & Cottaar, 2021), at least
 362 at X depths. We therefore broadly support the notion that plume signatures in the East
 363 African upper mantle are well mixed and the upper mantle pervasively hosts material
 364 transported from depth by the African Superplume (e.g., Rooney, 2017). However, we
 365 note that some scatter in X observations in East Africa may be associated with the vari-
 366 able presence of CO_2 assisted silicate melting that is required to explain the discrepancy
 367 between mantle potential temperature estimates and slow seismic wavespeeds below depths
 368 commonly associated with decompression melting (Rooney et al., 2012). Previous work-
 369 ers show the basal impedance contrast from such a carbonate silicate melt layer presents
 370 a viable explanation for the X (Dasgupta et al., 2013).

371 Moving southwards from Ethiopia, X observations terminate abruptly north of Lake
 372 Turkana (Figure 10) forming a WNW–ESE band of null observations that interrupt the
 373 broad trend of robust observations below the East African Rift. Given the presence of
 374 Quaternary volcanoes and Cenozoic magmatism in much of the Turkana Depression (Fig-
 375 ure 9), this result may indicate a locally different geodynamic environment to that ob-

376 served below the Ethiopian and East African plateaus beneath which two separate plumes
377 have been proposed (e.g., Pik et al., 2006). However, recent tomographic models present
378 no clear evidence for a break in slow wavespeeds (and therefore dynamic support) at the
379 upper mantle depths to which our data are sensitive (Hansen et al., 2012; Emry et al.,
380 2019; Celli, Lebedev, Schaeffer, & Gaina, 2020; Boyce et al., 2021; Kounoudis et al., 2021).
381 Intriguingly, a fast wavespeed band at lithospheric depths in southernmost Ethiopia in
382 the seismic tomographic study of Kounoudis et al. (2021), coincident with a broadly (~ 500 km-
383 wide) rifted zone (Figure 10) co-exists with our zone of absent X. This anomalous re-
384 gion, interpreted by Kounoudis et al. (2021) as refractory Proterozoic lithosphere, is not
385 associated with Quaternary volcanism, perhaps resulting in a lack of melt ponding be-
386 low the region at X depths. Complex lithospheric seismic structure, both associated with
387 the Kounoudis et al. (2021) fast wavespeed band, and with the failed Mesozoic Anza rift
388 immediately to the south of it in the Turkana Depression, may be precluding our view
389 of the X.

390 South of the Turkana Depression, the EARS splits into the ER, WR, Southwest-
391 ern and Southeastern rift zones (Figure 10a), which developed in Proterozoic lithosphere
392 between thick cratonic lithosphere (e.g., Chorowicz, 2005; Mulibo & Nyblade, 2016; Ebinger
393 et al., 2017; Daly et al., 2020). Owens et al. (2000) observe Pds arrivals at 250–300 km
394 across Tanzania, but they note that they cannot discriminate between a Pds phase or
395 a shallower multiple from velocity analysis alone. This region overlaps with regions of
396 X observations east of Lake Tanganyika along the WR and null observations due east
397 along the ER. Unlike the ER that has experienced 30 Ma-Recent magmatism along its
398 length, the WR is characterized by isolated, volumetrically small magmatic provinces
399 (e.g., Ebinger, 1989; Chorowicz, 2005; Roberts et al., 2012). The Southwestern rift zone
400 has no known magmatism, whereas the Southeastern rift zone offshore between Africa
401 and Madagascar has experienced ~ 20 Ma-recent magmatism (e.g., Michon, 2015; Cour-
402 geon et al., 2016, 2017; O’Connor et al., 2019; Berthod et al., 2022). Therefore, it is strik-
403 ing that the ER is underlain by null X observations while patchy X observations under-
404 lie the WR (Figure 9a). The two patches along the WR show consistent X depths of ~ 290 km,
405 however, at the surface, the northern patch is colocated with carbonatite magmatism
406 while the southern patch underlies no surface magmatism. Furthermore, the role of the
407 Tanzanian Craton, separating the two branches remains enigmatic. Whether through
408 edge-driven convection (King & Anderson, 1998; King & Ritsema, 2000) or lateral di-

409 version of plume material around the cratonic keel as suggested beneath the Kalahari
 410 Craton (Forte et al., 2010; Tepp et al., 2018), it remains uncertain whether the Tanza-
 411 nian Craton could divert chemically heterogeneous plume material to the WR. However,
 412 the Tanzanian Craton has a shallower depth extent than other cratons globally (e.g., Priest-
 413 ley et al., 2018; Celli, Lebedev, Schaeffer, & Gaina, 2020). Consequently, it is unclear
 414 whether it would have a similar impact on upper mantle flow compared to cratons of typ-
 415 ical thicknesses (≥ 250 km). Whether craton induced flow would result in our null obser-
 416 vation beneath the ER is also elusive.

417 **4.2.2 *Canaries***

418 Robust X observations occur at 270–280 km depth beneath the Canaries (Figure
 419 7a) with the most robust results appearing to the north and east (Figure 5). The Ca-
 420 naries have been shown to overlie a whole mantle plume in tomographic models (French
 421 & Romanowicz, 2015; Marignier et al., 2020), meaning, similarly to East Africa, the X
 422 beneath the Canaries may also result from the introduction of chemical heterogeneity
 423 from the deep mantle. Canarian shield stage lavas contain the signatures of both old (>1
 424 Ga; Thirlwall, 1997; Gurenko et al., 2006, 2009) and young (<1 Ga; Widom et al., 1999;
 425 Geldmacher & Hoernle, 2000) recycled oceanic crust. Should the Canarian mantle plume
 426 recycle oceanic crust to the surface, this may provide necessary chemical heterogeneity
 427 to explain the X via a single causal mechanism here, similar to other ocean island hotspots
 428 (e.g. Kemp et al., 2019; Pugh et al., 2021).

429 **4.2.3 *Morocco***

430 The X is widespread beneath Morocco. Observations of the X at 250–310 km depth
 431 (Figure 7a) show the greatest variation in depth over short spatial distances for our study
 432 region. Here the X has been observed in several previous studies (e.g. Deuss & Wood-
 433 house, 2002; Rein et al., 2020), with potential links to the Canaries mantle plume (e.g.
 434 Rein et al., 2020). We observed the X at depths of ~ 310 km on the western coastline shal-
 435 lowing monotonically eastwards to ~ 250 km (Figure 7a). However, to the south of this
 436 region, Rein et al. (2020) observe the X deepening \sim eastwards from ~ 310 km to ~ 350 km.
 437 Considering the Clapeyron slope of the Co-St phase transition invoked by Rein et al. (2020),
 438 it would be expected to deepen with increasing temperature. Wavespeed anomalies in
 439 this region in SEMUCB_WM1 and AF2019 transition from slow in the west, to fast in

440 the east. Interpreted in terms of temperature, this would suggest a cooling trend west
441 to east, and a shallowing X in line with our observations. Double X observations observed
442 in this region (Deuss & Woodhouse, 2002; Rein et al., 2020) may explain discrepancy
443 with our shallowing results. Although we do not observe two X observations, there is a
444 large standard deviation in X depth between stacks (Figure 7b). Large standard devi-
445 ation in depth is a reasonable indicator that two X observations may occur, often be-
446 ing collocated with two X observations elsewhere in the African continent (Figure 7), though
447 the secondary arrival may be a multiple.

448 Duggen et al. (2009) present geochemical analyses to show that the Canaries plume
449 may have deflected to the northeast beneath the Moroccan lithosphere, a suggestion sup-
450 ported by plume modelling (Mériaux et al., 2015). However, several studies (Lustrino
451 & Wilson, 2007; van den Bogaard, 2013) show that the geochemistry of magmatism across
452 the region does not fit with a single origin deep sourced mantle plume and is more read-
453 ily reconciled by multiple upper mantle upwellings. This remains a topic of ongoing de-
454 bate with a recent regional tomographic study suggesting that these multiple upwellings
455 may have a common deep source (Civiero et al., 2018). Rein et al. (2020) use evidence
456 of old and young recycled oceanic crust in lava samples from the Canaries (e.g., Thirl-
457 wall, 1997; Gurenko et al., 2006, 2009), and the proximity of subducted slabs in the Mediter-
458 ranean, to conclude that multiple upwellings recycle basalt into the upper mantle, fa-
459 cilitating the Co-St phase transition as the causal mechanism for the X. From our ex-
460 tended data set, it is possible that recycling of basalt may be pervasive across this re-
461 gion, extending offshore of Morocco beneath the Canaries.

462 *4.2.4 Cape Verde*

463 Shallow X observations are found to the south of Cape Verde and offshore Sene-
464 gal at 240–270 km depth, shallowing approximately north to south (Figure 7a). There
465 are also a number of doubled X observations in this region. X observations beneath Cape
466 Verde may be associated with hotspot magmatism and potentially also linked to the Ca-
467 naries plume. Whilst French and Romanowicz (2015) classify Cape Verde as overlying
468 a ‘primary plume’, Marignier et al. (2020) are less confident of a plume in this location
469 compared with the majority of their ‘primary plumes’. However, Cape Verde exhibits
470 HIMU and EM geochemical signatures, and high $^3\text{He}/^4\text{He}$ ratios (Doucelance et al., 2003;
471 Jackson et al., 2017, 2018), representing plume signatures. Geodynamic models (Davaille

472 et al., 2005) and precursor studies (Saki et al., 2015) found the Cape Verde plume to have
473 a common source in the lower mantle with the Canarian plume to the north. Should this
474 be the case, recycled basalt may be sourced from this singular upwelling ponded below
475 the 660 km discontinuity (e.g., Davaille et al., 2005).

476 **4.2.5 Hoggar**

477 We observe the X-discontinuity beneath the Hoggar mountains at 270–280 km depth,
478 deepening to the East (Figure 7a) where we find the most robust observations (Figure
479 5). While the X is present beneath Hoggar, its relationship to a potential mantle plume
480 is uncertain. In the hotspot catalogue of Courtillot et al. (2003), Hoggar has one of the
481 lowest probabilities of being a whole mantle plume (Marignier et al., 2020) and is clas-
482 sified as only ‘somewhat resolved’ by French and Romanowicz (2015). Further, the lavas
483 in Hoggar are characterized by MORB-like $^3\text{He}/^4\text{He}$ ratios (Pik et al., 2006; Jackson et
484 al., 2017) suggesting that they do not have a deep mantle source. The X is much deeper
485 than the 150 km source depth of magmatism (Liégeois et al., 2005), thus separate pro-
486 cesses may be invoked to explain the source of chemical heterogeneity and surface mag-
487 matism with little connection between the two. With limited station coverage it is dif-
488 ficult to assess the lateral extent of the X, and whether this observation is limited to the
489 Hoggar mountains alone, or whether it is connected to the widespread X observations
490 seen in Morocco.

491 **4.2.6 Cameroon**

492 Beneath Cameroon, we find the X colocated with the CVL. Robust X observations
493 are made in western Cameroon, decreasing in confidence eastwards from positive to neg-
494 ative normalized votes. X observations are made at 250–290 km depth.

495 There is much debate as to the source of magmatism along the CVL, meaning a
496 connection between magmatism and the X is uncertain here. Despite its linear morphol-
497 ogy and a HIMU signature consistent with a lower mantle source (Lee et al., 1994), there
498 is no age progression of magmatism along the CVL (e.g., Montigny et al., 2004). Fur-
499 ther, maximum $^3\text{He}/^4\text{He}$ ratios are not distinguishable from MORB ratios (Barfod et
500 al., 1999; Jackson et al., 2017). Continental and global tomographic models resolve a lower
501 mantle plume (e.g., French & Romanowicz, 2015), suggest that there may be some lower

502 mantle contribution to magmatism (Emry et al., 2019; Boyce et al., 2021), or classify the
 503 likelihood of a mantle plume as ‘unclear’ (Marignier et al., 2020). Previous MTZ and re-
 504 gional tomographic studies of the CVL do find evidence of a thermal anomaly across the
 505 MTZ (Reusch et al., 2010, 2011), favoring edge-driven convection as the source of mag-
 506 matism (King & Anderson, 1998; King & Ritsema, 2000). Other workers have also fa-
 507 vored non-plume, low melt volume mechanisms for CVL development (e.g., lithospheric
 508 delamination or fault zone reactivation: Milelli et al., 2012; Gallacher & Bastow, 2012;
 509 De Plaen et al., 2014; Fairhead & Binks, 1991).

510 Boyce and Cottaar (2021) find complex MTZ behavior in their recent study, with
 511 reduced 410 amplitudes, 20–30 km of thinning and variable 660 km discontinuity behav-
 512 ior. With mechanisms of a water-rich MTZ (Buchen et al., 2018) and a high basalt frac-
 513 tion (sufficient for X observation; Kemp et al., 2019) available to explain a disappear-
 514 ing 410 km discontinuity, Boyce and Cottaar (2021) do not preclude a lower mantle con-
 515 tribution to magmatism along the CVL. Should such a large basalt accumulation be present
 516 atop the 410 km discontinuity, the Co-St phase transition would be a likely candidate
 517 cause of the X in this region, as seen in Hawaii (Kemp et al., 2019). However, the depth
 518 of the X is much shallower here than the 336 km reported by Kemp et al. (2019) and such
 519 large basalt fractions remain unattainable in geodynamic models (Monaco et al., 2022).

520 **4.2.7 Madagascar**

521 X observations are present in two distinct patches across Madagascar. South-easternmost
 522 Madagascar is underlain by robust X observations at 270-280 km depth, with a strong
 523 band of null results through central Madagascar separating a less certain region of X ob-
 524 servations (normalized vote ≈ 0.5) to the north (Figures 5 and 7a).

525 Central and southern Madagascar are associated with substantial MTZ thinning
 526 and depression of both the 410 and 660 km discontinuities (Boyce & Cottaar, 2021), in-
 527 dicating a thermal upwelling across the MTZ. Recent tomographic studies image a low
 528 velocity anomaly extending from the surface beneath southernmost Madagascar to greater
 529 than 1000 km depth, connected to the African LLVP (Boyce et al., 2021; Tsekhmistrenko
 530 et al., 2021). Therefore, this anomaly maybe an upwelling branch of the African Super-
 531 plume. An upwelling from the lowermost mantle south of Madagascar would explain the
 532 sharp transition from null to robust X observations from north to south (Figure 5), but

533 it is unable to explain moderately certain X observations in central Madagascar that un-
534 derlie magmatism with a source depth at the base of the lithosphere (≤ 130 km; depth
535 Melluso et al., 2016).

536 Geochemical analyses of Cenozoic basalts in central Madagascar determine their
537 provenance to be the Madagascar continental mantle, with uplift, lithospheric thinning
538 and intercontinental rifting being the most likely processes to trigger melting (Melluso
539 et al., 2016; Cucciniello et al., 2017). Magma has been suggested to have spread later-
540 ally as far as Madagascar from the EARS along pre-existing structures like the Davie
541 ridge (Ebinger & Sleep, 1998; O’Connor et al., 2019). This is corroborated by plume-
542 like signatures and age progression of volcanics in the Comoros islands (Emerick & Dun-
543 can, 1982; Deniel, 1998). Owing to a lack of resolution offshore Mozambique, these re-
544 sults are unable to discriminate between these two models of melt generation. It is also
545 undetermined whether flow would be demarcated by X observations or whether this would
546 be constrained to the uppermost mantle.

547 **4.2.8 Mauritius and Réunion**

548 Mauritius and Réunion present two further hotspot ocean islands underlain by an
549 X. The X here is at 290–310 km depth, with the highest confidence southwest of Réunion
550 and decreasing eastwards of Mauritius.

551 While Marignier et al. (2020) find evidence of a mantle plume to be ‘unclear’ in
552 this region, French and Romanowicz (2015) find a plume to be ‘clearly resolved’ with high
553 $^3\text{He}/^4\text{He}$ ratios (Graham et al., 1990) corroborating a lower mantle source. Regional seis-
554 mic tomography reveals a slow wavespeed anomaly connected to the African LLVP (Tsekhmistrenko
555 et al., 2021). Though Tsekhmistrenko et al. (2021) invoke individual blobs episodically
556 detaching from the LLVP and subsequently ascending buoyantly, as opposed to a con-
557 tinuous plume conduit, this may provide a means to recycle basalt to the upper man-
558 tle in this region. Since plumes can only support a basalt fraction of 20% (Ballmer et
559 al., 2013; Dannberg & Sobolev, 2015), ponding of eclogite has been invoked to match the
560 seismically observable impedance contrasts of the X (Kemp et al., 2019). It is unclear
561 how individually ascending blobs would affect the amount of basalt available to pond
562 in the upper mantle.

563 **4.2.9 Southern Africa**

564 We largely observe a lack of the X in Southern Africa where the overlying litho-
 565 sphere comprises several cratons. Figure 11 shows an abrupt termination of X observa-
 566 tions at the margins of the Kalahari Craton which is characterized by high confidence
 567 null observations. As discussed before, it remains uncertain whether strong negative con-
 568 versions from the base of the craton mask weaker converted phases in RFs or whether
 569 there is indeed a lack of chemical heterogeneity/necessary geodynamic conditions to ob-
 570 serve the X beneath the thicker lithosphere extending to ≥ 200 km depth (e.g., Priest-
 571 ley et al., 2008; Fishwick, 2010; Adams & Nyblade, 2011).

572 In Pugh et al. (2021), six stacks beneath cratonic lithosphere from Canada, Brazil,
 573 Scandinavia, Siberia and Australia displayed null X observations to higher frequency than
 574 studied here, but strong negative conversions from the base of the craton still dominate
 575 the region for PXs conversions in depth and slowness stacks. Cooler than average man-
 576 tle temperatures may be expected beneath the base of the cratons in southern Africa,
 577 as evidenced by thickening of the MTZ by 10-20 km (Blum & Shen, 2004; Boyce & Cot-
 578 taar, 2021). This would raise the depth of the Co-St and OEN-HCEN transitions to ~ 250 km
 579 depth (Schmerr, 2015). While cool mantle temperatures are not observed beneath all
 580 cratons (e.g., Thompson et al., 2011), for the thicker cratons, this may inhibit phase tran-
 581 sitions associated with the X, preventing its observation (Figure S6). Additionally, in
 582 some locations, ponding of chemical heterogeneity may not be possible at the margins
 583 of the craton where complex flow is present due to edge-driven convection (King & An-
 584 derson, 1998; Currie & van Wijk, 2016).

585 **5 Conclusions**

586 X discontinuity structure beneath the African continent and surrounding ocean is-
 587 lands is vastly extended using widespread recordings of Pds RFs. The X is observed be-
 588 neath the EARS, Morocco, Cameroon, Hoggar and several ocean islands (Canaries, Cape
 589 Verde, Madagascar, Réunion and Mauritius) at 233–340 km depth using a normalized
 590 vote mapping approach.

591 The X is recorded across a broad range of depths and amplitudes. With no appar-
 592 ent relationship to upper mantle temperature and widespread occurrence across variable
 593 geodynamic settings, a multigenetic origin of the X is required below continents. Ob-

594 observations of the X are typically collocated with surface regions of Cenozoic magmatism
595 and Quaternary volcanoes, suggesting that surface magmatism is intrinsically linked to
596 upper mantle chemical heterogeneity, however some notable exceptions exist. The broad
597 connection may be explained by the presence of plumes of variable thermochemical na-
598 ture beneath parts/all of the EARS, the Canaries/Morocco, Cape Verde, southern Mada-
599 gascar and Réunion. However, it is difficult to explain the cause of upper mantle chem-
600 ical heterogeneity beneath Cameroon, Hoggar and central Madagascar by a plume re-
601 lated mechanism where upper mantle processes are mostly likely responsible for surface
602 magmatism. Whilst null observations dominate beneath cratons, it remains uncertain
603 if this is linked to localized geodynamic conditions (e.g., lack of chemical heterogeneity
604 or thermal anomaly) or is an artifact due to masking by shallower structure.

605 **Acknowledgments**

606 This project received funding from the Natural Environment Research Council (grant
607 number NE/L002507/1) awarded to S. Pugh, and the European Research Council (ERC)
608 under the European Union’s Horizon 2020 research and innovation program (grant agree-
609 ment No. 804071-ZoomDeep) awarded to S. Cottaar. C. J. Ebinger acknowledges NSFGEO-
610 NERC award 1824417. I. Bastow acknowledges support from Natural Environment Re-
611 search Council grant number NE/S014136/1.

612 **Open Research**

613 The facilities of IRIS Data Services, and specifically the IRIS Data Management
614 Center, alongside the AUSPASS, GEOFON, ORFEUS and RESIF data centres, were used
615 for access to waveforms, related metadata, and/or derived products used in this study.
616 IRIS Data Services are funded through the Seismological Facilities for the Advancement
617 of Geoscience (SAGE) Award of the National Science Foundation under Cooperative Sup-
618 port Agreement EAR-1851048. The waveform data used in this study are from the fol-
619 lowing networks: 1C (Velasco et al., 2011), 2H (Keir & Hammond, 2009), 2L (Lange &
620 Soler, 2019), 3D (Thomas, 2010), 4H (Hammond et al., 2011), 5H (Hammond, 2011), 6A
621 (Heit, Yuan, Jokat, et al., 2010), 6H (Helffrich & Fonseca, 2011), 6R (I. D. Bastow, 2019),
622 7C (Vergne et al., 2014), 8A (Nyblade, 2015a), 9A (Weber et al., 2007), 9C (Heit, Yuan,
623 & Mancilla, 2010), AF (Penn State University, 2004), G (Institut de physique du globe
624 de Paris (IPGP) & École et Observatoire des Sciences de la Terre de Strasbourg (EOST),

1982), GE (GEOFON Data Centre, 1993), GH (Ghana Geological Survey, 2012), GT (Albuquerque
 Seismological Laboratory (ASL)/USGS, 1993), IB (Institute Earth Sciences "Jaume Almera"
 CSIC (ICTJA Spain), 2007), II (Scripps Institution of Oceanography, 1986), IU (Albuquerque
 Seismological Laboratory (ASL)/USGS, 1988), IV (INGV Seismological Data Centre,
 1997), MN (MedNet Project Partner Institutions, 1988), NJ (Centre for Geodesy and
 Geodynamics, 2009), NR (Utrecht University (UU Netherlands), 1983), PF (Observatoire
 Volcanologique Du Piton De La Fournaise (OVPF) & Institut De Physique Du Globe
 De Paris (IPGP), 2008), PM (Instituto Português do Mar e da Atmosfera, I.P., 2006),
 TZ (Aubrey Adams, 2017), WM (San Fernando Royal Naval Observatory (ROA) et al.,
 1996), XA (Silver, 1997), XB (Wiens & Nyblade, 2005), XB (Levander et al., 2009), XC
 (Kind, 1998), XD (Owens & Nyblade, 1994), XI (Nyblade, 2000), XJ (Ebinger, 2013),
 XK (Gao et al., 2012), XM (The ARGOS Project, 2012), XV (Wysession et al., 2011),
 XW (Leroy et al., 2009), XW (Nyblade, 2017), Y1 (Ebinger, 2018), YA (Ebinger, 2012),
 YF (van der Lee et al., 1999), YH (Nyblade, 2010), YI (Gaherty & Shillington, 2010),
 YQ (Gaherty et al., 2013), YQ (Keir et al., 2017), YR (Levèque & RESIF, 2010), YV
 (Barruol et al., 2017), YY (Keranen, 2013), ZE (Ebinger, 2007), ZE (Tilmann et al., 2012),
 ZF (Fontaine et al., 2015), ZI (Wookey et al., 2011), ZK (Gao, 2009), ZP (Nyblade, 2007),
 ZS (Deschamps et al., 2007), ZT (Nyblade, 2015b) and ZV (Ebinger, 2014). Networks
 1B, BX, TT, XJ, XJ, XM, YF, YJ, YK, YW, YZ, ZC, ZF, ZP, ZQ and ZU do not have
 DOIs and are detailed in Table S1. This study uses ObsPy (Megies et al., 2011). Scripts
 for receiver function creation and processing are available through SMURFPy (Cottaar
 et al., 2020).

References

- Adams, A., & Nyblade, A. A. (2011). Shear wave velocity structure of the southern
 African upper mantle with implications for the uplift of southern Africa. *Geo-
 phys. J. Int.*, *186*(2), 808–824. Retrieved from <https://doi.org/10.1111/j.1365-246x.2011.05072.x> doi: 10.1111/j.1365-246x.2011.05072.x
- Akaogi, M., Oohata, M., Kojitani, H., & Kawaji, H. (2011). Thermodynamic
 properties of stishovite by low-temperature heat capacity measurements and
 the coesite-stishovite transition boundary. *Am. Mineral.*, *96*(8-9), 1325–
 1330. Retrieved from <https://doi.org/10.2138/am.2011.3748> doi:
 10.2138/am.2011.3748

- 657 Albuquerque Seismological Laboratory (ASL)/USGS. (1988). *Global Seismograph*
 658 *Network - IRIS/USGS*. International Federation of Digital Seismograph Net-
 659 works. Retrieved from <https://www.fdsn.org/networks/detail/IU/> doi: 10
 660 .7914/SN/IU
- 661 Albuquerque Seismological Laboratory (ASL)/USGS. (1993). *Global Telemetered*
 662 *Seismograph Network (USAF/USGS)*. International Federation of Digital
 663 Seismograph Networks. Retrieved from [https://www.fdsn.org/networks/](https://www.fdsn.org/networks/detail/GT/)
 664 [detail/GT/](https://www.fdsn.org/networks/detail/GT/) doi: 10.7914/SN/GT
- 665 Aubreya Adams. (2017). *Ol Doinyo Lengai, TZ Volcano Monitoring*. Interna-
 666 tional Federation of Digital Seismograph Networks. Retrieved from [https://](https://www.fdsn.org/networks/detail/TZ/)
 667 www.fdsn.org/networks/detail/TZ/ doi: 10.7914/SN/TZ
- 668 Ballmer, M. D., Ito, G., Wolfe, C. J., & Solomon, S. C. (2013). Double layering of a
 669 thermochemical plume in the upper mantle beneath Hawaii. *Earth Planet. Sci.*
 670 *Lett.*, *376*, 155–164. Retrieved from [https://doi.org/10.1016/j.epsl.2013](https://doi.org/10.1016/j.epsl.2013.06.022)
 671 [.06.022](https://doi.org/10.1016/j.epsl.2013.06.022) doi: 10.1016/j.epsl.2013.06.022
- 672 Barfod, D. N., Ballentine, C. J., Halliday, A. N., & Fitton, J. G. (1999). Noble
 673 gases in the cameroon line and the he, ne, and ar isotopic compositions of
 674 high μ (HIMU) mantle. *J. Geophys. Res. Solid Earth*, *104*(B12), 29509–
 675 29527. Retrieved from <https://doi.org/10.1029/1999jb900280> doi:
 676 10.1029/1999jb900280
- 677 Barruol, G., Sigloch, K., RHUM-RUM Group, & RESIF. (2017). *RHUM-RUM*
 678 *experiment, 2011-2015, code YV (Réunion Hotspot and Upper Mantle –*
 679 *Réunion's Unterer Mantel) funded by ANR, DFG, CNRS-INSU, IPEV, TAAF,*
 680 *instrumented by DEPAS, INSU-OBS, AWI and the Universities of Muenster,*
 681 *Bonn, La Réunion*. RESIF - Réseau Sismologique et géodésique Français.
 682 Retrieved from https://seismology.resif.fr/networks/#/YV_2011 doi:
 683 10.15778/RESIF.YV2011
- 684 Bastow, I., Nyblade, A., Stuart, G., Rooney, T., & Benoit, M. (2008). Upper Man-
 685 tle Seismic Structure Beneath the Ethiopian Hotspot: Rifting at the Edge of
 686 the African Low Velocity Anomaly. *Geochem. Geophys. Geosyst.*, *9*(12). doi:
 687 10.1029/2008GC002107
- 688 Bastow, I. D. (2019). *Turkana rift arrays to investigate lithospheric strains - uk com-*
 689 *ponent*. International Federation of Digital Seismograph Networks. Retrieved

- 690 from <https://www.fdsn.org/networks/detail/6R.2019/> doi: 10.7914/SN/
691 6R.2019
- 692 Begg, G., Griffin, W., Natapov, L., O'Reilly, S. Y., Grand, S., O'Neill, C., ... Bow-
693 den, P. (2009). The lithospheric architecture of Africa: Seismic tomography,
694 mantle petrology, and tectonic evolution. *Geosphere*, 5(1), 23-50. Retrieved
695 from <https://doi.org/10.1130/GES00179.1> doi: 10.1130/GES00179.1
- 696 Berthod, C., Bachelery, P., Jorry, S., Pitel-Roudaut, M., Ruffet, G., Revillon, S.,
697 ... Doucelance, R. (2022). First characterization of the volcanism in the
698 southern Mozambique Channel: Geomorphological and structural analy-
699 ses. *Mar. Geol.*, 445, 106755. Retrieved from [https://doi.org/10.1016/
700 j.margeo.2022.106755](https://doi.org/10.1016/j.margeo.2022.106755) doi: 10.1016/j.margeo.2022.106755
- 701 Bezada, M. J., Humphreys, E. D., Davila, J., Carbonell, R., Harnafi, M., Palomeras,
702 I., & Levander, A. (2014). Piecewise delamination of Moroccan lithosphere
703 from beneath the Atlas Mountains. *Geochem. Geophys. Geosyst.*, 15(4),
704 975–985. Retrieved from <https://doi.org/10.1002/2013gc005059> doi:
705 10.1002/2013gc005059
- 706 Bina, C. R., & Helffrich, G. (1994). Phase transition Clapeyron slopes and transition
707 zone seismic discontinuity topography. *J. Geophys. Res. Solid Earth*, 99(B8),
708 15853. Retrieved from <https://doi.org/10.1029/94jb00462> doi: 10.1029/
709 94jb00462
- 710 Blum, J., & Shen, Y. (2004). Thermal, hydrous, and mechanical states of the man-
711 tle transition zone beneath southern Africa. *Earth Planet. Sci. Lett.*, 217(3-4),
712 367–378. Retrieved from [https://doi.org/10.1016/s0012-821x\(03\)00628-9](https://doi.org/10.1016/s0012-821x(03)00628-9)
713 doi: 10.1016/s0012-821x(03)00628-9
- 714 Boyce, A., Bastow, I. D., Cottaar, S., Kounoudis, R., Courbeville, J. G. D., Caunt,
715 E., & Desai, S. (2021). AFRP20: New P-wavespeed model for the African
716 mantle reveals two whole-mantle plumes below East Africa and Neopro-
717 terozoic modification of the Tanzania craton. *Geochem. Geophys. Geosyst.*,
718 22(3). Retrieved from <https://doi.org/10.1029/2020gc009302> doi:
719 10.1029/2020gc009302
- 720 Boyce, A., & Cottaar, S. (2021). Insights into deep mantle thermochemical con-
721 tributions to African magmatism from converted seismic phases. *Geochem.*
722 *Geophys. Geosyst.*, 22(3). Retrieved from <https://doi.org/10.1029/>

- 723 2020gc009478 doi: 10.1029/2020gc009478
- 724 Buchen, J., Marquardt, H., Speziale, S., Kawazoe, T., Ballaran, T. B., & Kurnosov,
725 A. (2018). High-pressure single-crystal elasticity of wadsleyite and the seismic
726 signature of water in the shallow transition zone. *Earth Planet. Sci. Lett.*, *498*,
727 77–87. Retrieved from <https://doi.org/10.1016/j.epsl.2018.06.027> doi:
728 10.1016/j.epsl.2018.06.027
- 729 Celli, N. L., Lebedev, S., Schaeffer, A. J., & Gaina, C. (2020). African cra-
730 tonic lithosphere carved by mantle plumes. *Nat. Commun.*, *11*(1). Re-
731 trieved from <https://doi.org/10.1038/s41467-019-13871-2> doi:
732 10.1038/s41467-019-13871-2
- 733 Celli, N. L., Lebedev, S., Schaeffer, A. J., Ravenna, M., & Gaina, C. (2020). The
734 upper mantle beneath the South Atlantic Ocean, South America and Africa
735 from waveform tomography with massive data sets. *Geophys. J. Int.*, *221*(1),
736 178–204. Retrieved from <https://doi.org/10.1093/gji/ggz574> doi:
737 10.1093/gji/ggz574
- 738 Centre for Geodesy and Geodynamics. (2009). *Nigerian National Network of Seis-*
739 *mographic Stations (NNSS)*. International Federation of Digital Seismograph
740 Networks. Retrieved from <https://www.fdsn.org/networks/detail/NJ/>
741 doi: 10.7914/SN/NJ
- 742 Chang, S.-J., Ferreira, A. M., Ritsema, J., van Heijst, H. J., & Woodhouse, J. H.
743 (2015). Joint inversion for global isotropic and radially anisotropic man-
744 tle structure including crustal thickness perturbations. *J. Geophys. Res.*
745 *Solid Earth*, *120*(6), 4278–4300. Retrieved from [https://doi.org/10.1002/](https://doi.org/10.1002/2014JB011824)
746 [2014JB011824](https://doi.org/10.1002/2014JB011824) doi: 10.1002/2014JB011824
- 747 Chang, S.-J., Kendall, E., Davaille, A., & Ferreira, A. M. G. (2020). The evo-
748 lution of mantle plumes in East Africa. *J. Geophys. Res. Solid Earth*,
749 *125*(12). Retrieved from <https://doi.org/10.1029/2020jb019929> doi:
750 10.1029/2020jb019929
- 751 Chorowicz, J. (2005). The East African rift system. *J. Afr. Earth Sci.*, *43*(1-3), 379–
752 410. Retrieved from <https://doi.org/10.1016/j.jafrearsci.2005.07.019>
753 doi: 10.1016/j.jafrearsci.2005.07.019
- 754 Civiero, C., Goes, S., Hammond, J. O., Fishwick, S., Ahmed, A., Ayele, A., . . . oth-
755 ers (2016). Small-scale thermal upwellings under the northern East African

- 756 Rift from S travel time tomography. *J. Geophys. Res. Solid Earth*, 121(10),
 757 7395–7408. Retrieved from <https://doi.org/10.1002/2016JB013070> doi:
 758 10.1002/2016JB013070
- 759 Civiero, C., Hammond, J. O., Goes, S., Fishwick, S., Ahmed, A., Ayele, A., ...
 760 others (2015). Multiple mantle upwellings in the transition zone beneath
 761 the northern East-African Rift system from relative P-wave travel-time to-
 762 mography. *Geochem. Geophys. Geosyst.*, 16(9), 2949–2968. Retrieved from
 763 <https://doi.org/10.1002/2015GC005948> doi: 10.1002/2015GC005948
- 764 Civiero, C., Strak, V., Custódio, S., Silveira, G., Rawlinson, N., Arroucau, P., &
 765 Corela, C. (2018). A common deep source for upper-mantle upwellings be-
 766 low the Ibero-western Maghreb region from teleseismic P-wave travel-time
 767 tomography. *Earth Planet. Sci. Lett.*, 499, 157–172. Retrieved from [https://](https://doi.org/10.1016/j.epsl.2018.07.024)
 768 doi.org/10.1016/j.epsl.2018.07.024 doi: 10.1016/j.epsl.2018.07.024
- 769 Cottaar, S., & Deuss, A. (2016). Large-scale mantle discontinuity topography be-
 770 neath Europe: Signature of akimotoite in subducting slabs. *J. Geophys. Res.*
 771 *Solid Earth*, 121(1), 279–292. Retrieved from [https://doi.org/10.1002/](https://doi.org/10.1002/2015jb012452)
 772 [2015jb012452](https://doi.org/10.1002/2015jb012452) doi: 10.1002/2015jb012452
- 773 Cottaar, S., Pugh, S., Boyce, A., & Jenkins, J. (2020). *sannecottaar/smurfpy*:
 774 *SMURFPy*. Zenodo. Retrieved from <https://zenodo.org/record/4337258>
 775 doi: 10.5281/ZENODO.4337258
- 776 Courgeon, S., Jorry, S., Camoin, G., BouDagher-Fadel, M., Jouet, G., Révillon, S.,
 777 ... Droxler, A. (2016). Growth and demise of Cenozoic isolated carbonate
 778 platforms: New insights from the Mozambique Channel seamounts (SW Indian
 779 Ocean). *Mar. Geol.*, 380, 90–105. Retrieved from [https://doi.org/10.1016/](https://doi.org/10.1016/j.margeo.2016.07.006)
 780 [j.margeo.2016.07.006](https://doi.org/10.1016/j.margeo.2016.07.006) doi: 10.1016/j.margeo.2016.07.006
- 781 Courgeon, S., Jorry, S., Jouet, G., Camoin, G., BouDagher-Fadel, M., Bachèlery, P.,
 782 ... Guérin, C. (2017). Impact of tectonic and volcanism on the Neogene evolu-
 783 tion of isolated carbonate platforms (SW Indian Ocean). *Sediment. Geol.*, 355,
 784 114–131. Retrieved from <https://doi.org/10.1016/j.sedgeo.2017.04.008>
 785 doi: 10.1016/j.sedgeo.2017.04.008
- 786 Courtillot, V., Davaille, A., Besse, J., & Stock, J. (2003). Three distinct types of
 787 hotspots in the Earth's mantle. *Earth Planet. Sci. Lett.*, 205(3-4), 295–308.
 788 Retrieved from [https://doi.org/10.1016/s0012-821x\(02\)01048-8](https://doi.org/10.1016/s0012-821x(02)01048-8) doi:

789 10.1016/s0012-821x(02)01048-8

790 Croftwell, H. P., Owens, T. J., & Ritsema, J. (1999). The TauP toolkit: Flexible seis-
791 mic travel-time and ray-path utilities. *Seis. Res. Lett.*, *70*(2), 154–160. Re-
792 trieved from <https://doi.org/10.1785/gssrl.70.2.154> doi: 10.1785/gssrl
793 .70.2.154

794 Cucciniello, C., Melluso, L., le Roex, A. P., Jourdan, F., Morra, V., de' Gennaro,
795 R., & Grifa, C. (2017). From olivine nephelinite, basanite and basalt
796 to peralkaline trachyphonolite and comendite in the Ankaratra volcanic
797 complex, Madagascar: 40 Ar/ 39 Ar ages, phase compositions and bulk-
798 rock geochemical and isotopic evolution. *Lithos*, *274-275*, 363–382. Re-
799 trieved from <https://doi.org/10.1016/j.lithos.2016.12.026> doi:
800 10.1016/j.lithos.2016.12.026

801 Currie, C. A., & van Wijk, J. (2016). How craton margins are preserved: Insights
802 from geodynamic models. *J. Geodyn.*, *100*, 144–158. Retrieved from [https://](https://doi.org/10.1016/j.jog.2016.03.015)
803 doi.org/10.1016/j.jog.2016.03.015 doi: 10.1016/j.jog.2016.03.015

804 Daly, M. C., Green, P., Watts, A. B., Davies, O., Chibesakunda, F., & Walker, R.
805 (2020). Tectonics and landscape of the Central African Plateau and their im-
806 plications for a propagating Southwestern Rift in Africa. *Geochem. Geophys.*
807 *Geosyst.*, *21*(6). Retrieved from <https://doi.org/10.1029/2019gc008746>
808 doi: 10.1029/2019gc008746

809 Dannberg, J., & Sobolev, S. V. (2015). Low-buoyancy thermochemical plumes
810 resolve controversy of classical mantle plume concept. *Nat. Commun.*,
811 *6*(1). Retrieved from <https://doi.org/10.1038/ncomms7960> doi:
812 10.1038/ncomms7960

813 Dasgupta, R., Mallik, A., Tsuno, K., Withers, A. C., Hirth, G., & Hirschmann,
814 M. M. (2013). Carbon-dioxide-rich silicate melt in the Earth's upper mantle.
815 *Nature*, *493*(7431), 211–215. Retrieved from [https://doi.org/10.1038/](https://doi.org/10.1038/nature11731)
816 [nature11731](https://doi.org/10.1038/nature11731) doi: 10.1038/nature11731

817 Davaille, A., Stutzmann, E., Silveira, G., Besse, J., & Courtillot, V. (2005). Con-
818 vective patterns under the Indo-Atlantic « box ». *Earth Planet. Sci. Lett.*,
819 *239*(3-4), 233–252. Retrieved from <https://doi.org/10.1016/j.epsl.2005.07.024>
820 .07.024 doi: 10.1016/j.epsl.2005.07.024

821 De Plaen, R. S. M., Bastow, I. D., Chambers, E. L., Keir, D., Gallacher, R. J., &

- 822 Keane, J. (2014). The development of magmatism along the Cameroon Vol-
 823 canic Line: Evidence from seismicity and seismic anisotropy. *J. Geophys. Res.*
 824 *Solid Earth*, 119(5), 4233–4252. Retrieved from [https://doi.org/10.1002/](https://doi.org/10.1002/2013jb010583)
 825 2013jb010583 doi: 10.1002/2013jb010583
- 826 Debayle, E., Dubuffet, F., & Durand, S. (2016). An automatically updated s-wave
 827 model of the upper mantle and the depth extent of azimuthal anisotropy. *Geo-*
 828 *phys. Res. Lett.*, 43(2), 674–682.
- 829 de Gouveia, S. V., Besse, J., de Lamotte, D. F., Greff-Lefftz, M., Lescanne, M.,
 830 Gueydan, F., & Leparmentier, F. (2018). Evidence of hotspot paths below
 831 Arabia and the Horn of Africa and consequences on the Red Sea opening.
 832 *Earth Planet. Sci. Lett.*, 487, 210–220. Retrieved from [https://doi.org/](https://doi.org/10.1016/j.epsl.2018.01.030)
 833 10.1016/j.epsl.2018.01.030 doi: 10.1016/j.epsl.2018.01.030
- 834 Deniel, C. (1998). Geochemical and isotopic (Sr, Nd, Pb) evidence for plume-
 835 lithosphere interactions in the genesis of Grande Comore magmas (Indian
 836 Ocean). *Chem. Geol.*, 144(3-4), 281–303. Retrieved from [https://doi.org/](https://doi.org/10.1016/s0009-2541(97)00139-3)
 837 10.1016/s0009-2541(97)00139-3 doi: 10.1016/s0009-2541(97)00139-3
- 838 Déruelle, B., Moreau, C., Nkoumbou, C., Kambou, R., Lissom, J., Njonfang, E.,
 839 ... Nono, A. (1991). The Cameroon Line: A review. In *Magmatism in*
 840 *extensional structural settings* (pp. 274–327). Springer Berlin Heidelberg.
 841 Retrieved from https://doi.org/10.1007/978-3-642-73966-8_12 doi:
 842 10.1007/978-3-642-73966-8_12
- 843 Deschamps, A., Déverchère, J., & Ferdinand, R. (2007). *SEISMOTANZ'07. RE-*
 844 *SIF - Réseau Sismologique et géodésique Français*. Retrieved from [https://](https://seismology.resif.fr/networks/#/ZS_2007)
 845 seismology.resif.fr/networks/#/ZS_2007 doi: 10.15778/RESIF.ZS2007
- 846 Deuss, A., & Woodhouse, J. H. (2002). A systematic search for mantle disconti-
 847 nities using ss-precursors. *Geophys. Res. Lett.*, 29(8), 90–1. Retrieved from
 848 <https://doi.org/10.1029/2002GL014768> doi: 10.1029/2002GL014768
- 849 Deuss, A., & Woodhouse, J. H. (2004). The nature of the Lehmann discontinuity
 850 from its seismological Clapeyron slopes. *Earth Planet. Sci. Lett.*, 225(3-4),
 851 295–304. Retrieved from <https://doi.org/10.1016/j.epsl.2004.06.021>
 852 doi: 10.1016/j.epsl.2004.06.021
- 853 Doucelance, R., Escrig, S., Moreira, M., Gariépy, C., & Kurz, M. D. (2003).
 854 Pb-sr-he isotope and trace element geochemistry of the cape verde

- 855 archipelago. *Geochim. Cosmochim. Acta.*, 67(19), 3717–3733. Re-
 856 trieved from [https://doi.org/10.1016/s0016-7037\(03\)00161-3](https://doi.org/10.1016/s0016-7037(03)00161-3) doi:
 857 10.1016/s0016-7037(03)00161-3
- 858 Dueker, K. G., & Sheehan, A. F. (1997). Mantle discontinuity structure from mid-
 859 point stacks of converted p to s waves across the yellowstone hotspot track. *J.*
 860 *Geophys. Res. Solid Earth*, 102(B4), 8313–8327. Retrieved from [https://doi](https://doi.org/10.1029/96JB03857)
 861 [.org/10.1029/96JB03857](https://doi.org/10.1029/96JB03857) doi: 10.1029/96JB03857
- 862 Dueker, K. G., & Sheehan, A. F. (1998). Mantle discontinuity structure beneath
 863 the colorado rocky mountains and high plains. *J. Geophys. Res. Solid Earth*,
 864 103(B4), 7153–7169. Retrieved from <https://doi.org/10.1029/97jb03509>
 865 doi: 10.1029/97jb03509
- 866 Duggen, S., Hoernle, K., Hauff, F., Klügel, A., Bouabdellah, M., & Thirlwall, M.
 867 (2009). Flow of Canary mantle plume material through a subcontinental
 868 lithospheric corridor beneath Africa to the Mediterranean. *Geology*, 37(3),
 869 283–286. Retrieved from <https://doi.org/10.1130/g25426a.1> doi:
 870 10.1130/g25426a.1
- 871 Dziewonski, A. M., & Anderson, D. L. (1981). Preliminary reference Earth model.
 872 *Phys. Earth Planet. Int.*, 25(4), 297–356. Retrieved from [https://doi.org/10](https://doi.org/10.1016/0031-9201(81)90046-7)
 873 [.1016/0031-9201\(81\)90046-7](https://doi.org/10.1016/0031-9201(81)90046-7) doi: 10.1016/0031-9201(81)90046-7
- 874 Ebinger, C. J. (1989). Tectonic development of the western branch of the East
 875 African rift system. *Geol. Soc. Am.*, 101(7), 885–903. Retrieved from
 876 [https://doi.org/10.1130/0016-7606\(1989\)101<0885:TDOTWB>2.3.CO;2](https://doi.org/10.1130/0016-7606(1989)101<0885:TDOTWB>2.3.CO;2)
 877 doi: 10.1130/0016-7606(1989)101(0885:TDOTWB)2.3.CO;2
- 878 Ebinger, C. J. (2007). *AFAR07*. International Federation of Digital Seismo-
 879 graph Networks. Retrieved from [https://www.fdsn.org/networks/detail/](https://www.fdsn.org/networks/detail/ZE_2007/)
 880 [ZE_2007/](https://www.fdsn.org/networks/detail/ZE_2007/) doi: 10.7914/SN/ZE_2007
- 881 Ebinger, C. J. (2012). *Dynamics of the Lake Kivu System*. International Fed-
 882 eration of Digital Seismograph Networks. Retrieved from [https://www.fdsn](https://www.fdsn.org/networks/detail/YA_2012/)
 883 [.org/networks/detail/YA_2012/](https://www.fdsn.org/networks/detail/YA_2012/) doi: 10.7914/SN/YA_2012
- 884 Ebinger, C. J. (2013). *Magadi-Natron magmatic rifting studies*. International Fed-
 885 eration of Digital Seismograph Networks. Retrieved from [https://www.fdsn](https://www.fdsn.org/networks/detail/XJ_2013/)
 886 [.org/networks/detail/XJ_2013/](https://www.fdsn.org/networks/detail/XJ_2013/) doi: 10.7914/SN/XJ_2013
- 887 Ebinger, C. J. (2014). *Southern Lake Tanganyika experiment*. International Fed-

- 888 eration of Digital Seismograph Networks. Retrieved from [https://www.fdsn](https://www.fdsn.org/networks/detail/ZV_2014/)
889 [.org/networks/detail/ZV_2014/](https://www.fdsn.org/networks/detail/ZV_2014/) doi: 10.7914/SN/ZV_2014
- 890 Ebinger, C. J. (2018). *Crust and mantle structure and the expression of extension*
891 *in the Turkana depression of Kenya and Ethiopia.* International Federation
892 of Digital Seismograph Networks. Retrieved from [https://www.fdsn.org/](https://www.fdsn.org/networks/detail/Y1_2018/)
893 [networks/detail/Y1_2018/](https://www.fdsn.org/networks/detail/Y1_2018/) doi: 10.7914/SN/Y1_2018
- 894 Ebinger, C. J., Keir, D., Bastow, I. D., Whaler, K., Hammond, J. O. S., Ayele,
895 A., . . . Hautot, S. (2017). Crustal structure of active deformation zones in
896 Africa: Implications for global crustal processes. *Tectonics*, *36*(12), 3298–
897 3332. Retrieved from <https://doi.org/10.1002/2017tc004526> doi:
898 10.1002/2017tc004526
- 899 Ebinger, C. J., & Sleep, N. H. (1998). Cenozoic magmatism throughout east africa
900 resulting from impact of a single plume. *Nature*, *395*(6704), 788–791. Re-
901 trieved from <https://doi.org/10.1038/27417> doi: 10.1038/27417
- 902 Emerick, C., & Duncan, R. (1982). Age progressive volcanism in the Comores
903 Archipelago, western Indian Ocean and implications for Somali plate tectonics.
904 *Earth Planet. Sci. Lett.*, *60*(3), 415–428. Retrieved from [https://doi.org/](https://doi.org/10.1016/0012-821x(82)90077-2)
905 [10.1016/0012-821x\(82\)90077-2](https://doi.org/10.1016/0012-821x(82)90077-2) doi: 10.1016/0012-821x(82)90077-2
- 906 Emry, E. L., Shen, Y., Nyblade, A. A., Flinders, A., & Bao, X. (2019). Up-
907 per Mantle Earth Structure in Africa From Full-Wave Ambient Noise To-
908 mography. *Geochem. Geophys. Geosyst.*, *20*(1), 120–147. Retrieved from
909 <https://doi.org/10.1029/2018gc007804> doi: 10.1029/2018gc007804
- 910 Fairhead, J., & Binks, R. (1991). Differential Opening of the Central and South
911 Atlantic Oceans and the Opening of the West African Rift System. *Tectono-*
912 *physics*, *187*(1-3), 191–203.
- 913 Fishwick, S. (2010). Surface wave tomography: Imaging of the lithosphere-
914 asthenosphere boundary beneath central and southern Africa? *Lithos*, *120*(1-
915 2), 63–73. Retrieved from <https://doi.org/10.1016/j.lithos.2010.05.011>
916 doi: 10.1016/j.lithos.2010.05.011
- 917 Fitton, J. (1980). The Benue trough and Cameroon Line — A migrating rift
918 system in West Africa. *Earth Planet. Sci. Lett.*, *51*(1), 132–138. Re-
919 trieved from [https://doi.org/10.1016/0012-821x\(80\)90261-7](https://doi.org/10.1016/0012-821x(80)90261-7) doi:
920 10.1016/0012-821x(80)90261-7

- 921 Fontaine, F. R., Barruol, G., & Gonzalez, A. (2015). *Rivière des Pluies Project,*
 922 *La Réunion Island, 2015-2018.* RESIF - Réseau Sismologique et géodésique
 923 Français. Retrieved from [https://seismology.resif.fr/networks/#/](https://seismology.resif.fr/networks/#/ZF_2015)
 924 ZF_2015 doi: 10.15778/RESIF.ZF2015
- 925 Forte, A. M., Quéré, S., Moucha, R., Simmons, N. A., Grand, S. P., Mitrovica, J. X.,
 926 & Rowley, D. B. (2010). Joint seismic-geodynamic-mineral physical mod-
 927 elling of African geodynamics: A reconciliation of deep-mantle convection
 928 with surface geophysical constraints. *Earth Planet. Sci. Lett.*, 295(3-4), 329–
 929 341. Retrieved from <https://doi.org/10.1016/j.epsl.2010.03.017> doi:
 930 10.1016/j.epsl.2010.03.017
- 931 French, S. W., & Romanowicz, B. (2015). Broad plumes rooted at the base of the
 932 Earth's mantle beneath major hotspots. *Nature*, 525(7567), 95–99. Retrieved
 933 from <https://doi.org/10.1038/nature14876> doi: 10.1038/nature14876
- 934 French, S. W., & Romanowicz, B. A. (2014). Whole-mantle radially anisotropic
 935 shear velocity structure from spectral-element waveform tomography. *Geophys.*
 936 *J. Int.*, 199(3), 1303–1327. Retrieved from [https://doi.org/10.1093/gji/](https://doi.org/10.1093/gji/ggu334)
 937 [ggu334](https://doi.org/10.1093/gji/ggu334) doi: 10.1093/gji/ggu334
- 938 Fullea, J., Lebedev, S., Martinec, Z., & Celli, N. L. (2021). WINTERC-g: mapping
 939 the upper mantle thermochemical heterogeneity from coupled geophysical-
 940 petrological inversion of seismic waveforms, heat flow, surface elevation and
 941 gravity satellite data. *Geophys. J. Int.*, 226(1), 146–191. Retrieved from
 942 <https://doi.org/10.1093/gji/ggab094> doi: 10.1093/gji/ggab094
- 943 Furman, T., Bryce, J., Rooney, T., Hanan, B., Yirgu, G., & Ayalew, D. (2006).
 944 Heads and tails: 30 million years of the Afar plume. *Geological Society, Lon-*
 945 *don, Special Publications*, 259(1), 95–119. Retrieved from [https://doi.org/](https://doi.org/10.1144/gsl.sp.2006.259.01.09)
 946 [10.1144/gsl.sp.2006.259.01.09](https://doi.org/10.1144/gsl.sp.2006.259.01.09) doi: 10.1144/gsl.sp.2006.259.01.09
- 947 Gaherty, J., Ebinger, C. J., Nyblade, A. A., & Shillington, D. (2013). *Study of*
 948 *extension and magmatism in Malawi and Tanzania.* International Federation
 949 of Digital Seismograph Networks. Retrieved from [https://www.fdsn.org/](https://www.fdsn.org/networks/detail/YQ_2013/)
 950 [networks/detail/YQ_2013/](https://www.fdsn.org/networks/detail/YQ_2013/) doi: 10.7914/SN/YQ_2013
- 951 Gaherty, J., & Shillington, D. (2010). *2009 Malawi Earthquake RAMP Re-*
 952 *sponse.* International Federation of Digital Seismograph Networks. Re-
 953 trieved from https://www.fdsn.org/networks/detail/YI_2010/ doi:

954 10.7914/SN/YI.2010

955 Gallacher, R., & Bastow, I. (2012). The Development of Magmatism Along the
956 Cameroon Volcanic Line: Evidence from Teleseismic Receiver Functions. *Tec-*
957 *tonics*, 31. doi: 10.1029/2011TC003028

958 Gao, S. (2009). *Afar depression dense seismic array*. International Federation
959 of Digital Seismograph Networks. Retrieved from [https://www.fdsn.org/
960 networks/detail/ZK_2009/](https://www.fdsn.org/networks/detail/ZK_2009/) doi: 10.7914/SN/ZK.2009

961 Gao, S., Liu, K., Abdelsalam, M., & Hogan, J. (2012). *Seismic arrays for African*
962 *Rift initiation*. International Federation of Digital Seismograph Networks.
963 Retrieved from https://www.fdsn.org/networks/detail/XK_2012/ doi:
964 10.7914/SN/XK.2012

965 Geldmacher, J., & Hoernle, K. (2000). The 72 Ma geochemical evolution of the
966 Madeira hotspot (eastern North Atlantic): recycling of Paleozoic (≤ 500
967 Ma) oceanic lithosphere. *Earth Planet. Sci. Lett.*, 183(1-2), 73–92. Re-
968 trieved from [https://doi.org/10.1016/S0012-821X\(00\)00266-1](https://doi.org/10.1016/S0012-821X(00)00266-1) doi:
969 10.1016/S0012-821X(00)00266-1

970 GEOFON Data Centre. (1993). *GEOFON Seismic Network*. Deutsches Geo-
971 Forschungszentrum GFZ. Retrieved from [http://geofon.gfz-potsdam.de/
972 doi/network/GE](http://geofon.gfz-potsdam.de/doi/network/GE) doi: 10.14470/TR560404

973 Ghana Geological Survey. (2012). *Ghana digital seismic network*. International Fed-
974 eration of Digital Seismograph Networks. Retrieved from [https://www.fdsn
975 .org/networks/detail/GH/](https://www.fdsn.org/networks/detail/GH/) doi: 10.7914/SN/GH

976 Graham, D., Lupton, J., Albarède, F., & Condomines, M. (1990). Extreme tem-
977 poral homogeneity of helium isotopes at piton de la fournaise, réunion island.
978 *Nature*, 347(6293), 545–548. Retrieved from [https://doi.org/10.1038/
979 347545a0](https://doi.org/10.1038/347545a0) doi: 10.1038/347545a0

980 Gurenko, A. A., Hoernle, K. A., Hauff, F., Schmincke, H.-U., Han, D., Miura, Y. N.,
981 & Kaneoka, I. (2006). Major, trace element and Nd-Sr-Pb-O-He-Ar isotope
982 signatures of shield stage lavas from the central and western Canary Islands:
983 Insights into mantle and crustal processes. *Chem. Geol.*, 233(1-2), 75–112.
984 Retrieved from <https://doi.org/10.1016/j.chemgeo.2006.02.016> doi:
985 10.1016/j.chemgeo.2006.02.016

986 Gurenko, A. A., Sobolev, A. V., Hoernle, K. A., Hauff, F., & Schmincke, H.-U.

- 987 (2009). Enriched, HIMU-type peridotite and depleted recycled pyroxenite in
 988 the Canary plume: A mixed-up mantle. *Earth Planet. Sci. Lett.*, 277(3-4),
 989 514–524. Retrieved from <https://doi.org/10.1016/j.epsl.2008.11.013>
 990 doi: 10.1016/j.epsl.2008.11.013
- 991 Hammond, J. (2011). *Eritrea seismic project*. International Federation of Digital
 992 Seismograph Networks. Retrieved from [https://www.fdsn.org/networks/
 993 detail/5H.2011/](https://www.fdsn.org/networks/detail/5H.2011/) doi: 10.7914/SN/5H.2011
- 994 Hammond, J., Goitom, B., Kendall, J. M., & Ogubazghi, G. (2011). *Nabro urgency*
 995 *array*. International Federation of Digital Seismograph Networks. Retrieved
 996 from <https://www.fdsn.org/networks/detail/4H.2011/> doi: 10.7914/SN/
 997 4H.2011
- 998 Hansen, S. E., Nyblade, A. A., & Benoit, M. H. (2012). Mantle structure beneath
 999 Africa and Arabia from adaptively parameterized P-wave tomography: Impli-
 1000 cations for the origin of Cenozoic Afro-Arabian tectonism. *Earth Planet. Sci.*
 1001 *Lett.*, 319, 23–34. doi: 10.1016/j.epsl.2011.12.023
- 1002 Heit, B., Yuan, X., Jokat, W., Weber, M., & Geissler, W. (2010). *WALPASS Net-*
 1003 *work, Namibia, 2010/2012*. Deutsches GeoForschungsZentrum GFZ. Retrieved
 1004 from <http://geofon.gfz-potsdam.de/doi/network/6A/2010> doi: 10.14470/
 1005 1N134371
- 1006 Heit, B., Yuan, X., & Mancilla, F. D. L. (2010). *High resolution seismological profil-*
 1007 *ing across Sierra Nevada (HIRE)*. Deutsches GeoForschungsZentrum GFZ. Re-
 1008 trieved from <http://geofon.gfz-potsdam.de/doi/network/9C/2010> doi: 10
 1009 .14470/4P7565788335
- 1010 Helffrich, G. (2000). Topography of the transition zone seismic discontinuities.
 1011 *Rev. Geophys.*, 38(1), 141–158. Retrieved from [https://doi.org/10.1029/
 1012 1999rg000060](https://doi.org/10.1029/1999rg000060) doi: 10.1029/1999rg000060
- 1013 Helffrich, G. (2002). Thermal variations in the mantle inferred from 660 km
 1014 discontinuity topography and tomographic wave speed variations. *Geo-*
 1015 *phys. J. Int.*, 151(3), 935–943. Retrieved from [https://doi.org/10.1046/
 1016 j.1365-246x.2002.01824.x](https://doi.org/10.1046/j.1365-246x.2002.01824.x) doi: 10.1046/j.1365-246x.2002.01824.x
- 1017 Helffrich, G., & Fonseca, J. F. B. D. (2011). *Mozambique rift tomography*. Interna-
 1018 tional Federation of Digital Seismograph Networks. Retrieved from [https://
 1019 www.fdsn.org/networks/detail/6H.2011/](https://www.fdsn.org/networks/detail/6H.2011/) doi: 10.7914/SN/6H.2011

- 1020 Ho, T., Priestley, K., & Debayle, E. (2016). A global horizontal shear velocity model
 1021 of the upper mantle from multimode love wave measurements. *Geophys. J.*
 1022 *Int.*, 207(1), 542–561. Retrieved from <https://doi.org/10.1093/gji/ggw292>
 1023 doi: 10.1093/gji/ggw292
- 1024 Hoggard, M. J., Czarnota, K., Richards, F. D., Huston, D. L., Jaques, A. L., &
 1025 Ghelichkhan, S. (2020). Global distribution of sediment-hosted met-
 1026 als controlled by craton edge stability. *Nat. Geosci.*, 13(7), 504–510.
 1027 Retrieved from <https://doi.org/10.1038/s41561-020-0593-2> doi:
 1028 10.1038/s41561-020-0593-2
- 1029 INGV Seismological Data Centre. (1997). *Rete Sismica Nazionale (RSN)*. Isti-
 1030 tuto Nazionale di Geofisica e Vulcanologia (INGV), Italy. Retrieved from
 1031 <http://cnt.rm.ingv.it/instruments/network/IV> doi: 10.13127/SD/
 1032 X0FXNH7QFY
- 1033 Institut de physique du globe de Paris (IPGP), & École et Observatoire des Sciences
 1034 de la Terre de Strasbourg (EOST). (1982). *GEOSCOPE, French Global Net-*
 1035 *work of broad band seismic stations*. Institut de physique du globe de Paris
 1036 (IPGP), Université de Paris. Retrieved from [http://geoscope.ipgp.fr/](http://geoscope.ipgp.fr/networks/detail/G/)
 1037 [networks/detail/G/](http://geoscope.ipgp.fr/networks/detail/G/) doi: 10.18715/GEOSCOPE.G
- 1038 Institute Earth Sciences "Jaume Almera" CSIC (ICTJA Spain). (2007). *IberAr-*
 1039 *ray*. International Federation of Digital Seismograph Networks. Retrieved from
 1040 <https://www.fdsn.org/networks/detail/IB/> doi: 10.7914/SN/IB
- 1041 Instituto Português do Mar e da Atmosfera, I.P. (2006). *Portuguese National*
 1042 *Seismic Network*. International Federation of Digital Seismograph Net-
 1043 works. Retrieved from <https://www.fdsn.org/networks/detail/PM/> doi:
 1044 10.7914/SN/PM
- 1045 Jackson, M. G., Becker, T., & Konter, J. (2018). Evidence for a deep mantle source
 1046 for EM and HIMU domains from integrated geochemical and geophysical con-
 1047 straints. *Earth Planet. Sci. Lett.*, 484, 154–167. Retrieved from [https://](https://doi.org/10.1016/j.epsl.2017.11.052)
 1048 doi.org/10.1016/j.epsl.2017.11.052 doi: 10.1016/j.epsl.2017.11.052
- 1049 Jackson, M. G., Konter, J. G., & Becker, T. (2017). Primordial helium entrained
 1050 by the hottest mantle plumes. *Nature*, 542(7641), 340–343. Retrieved from
 1051 <https://doi.org/10.1038/nature21023> doi: 10.1038/nature21023
- 1052 Jenkins, J., Cottaar, S., White, R., & Deuss, A. (2016). Depressed mantle disconti-

- 1053 nities beneath Iceland: Evidence of a garnet controlled 660 km discontinuity?
 1054 *Earth Planet. Sci. Lett.*, *433*, 159–168. Retrieved from [https://doi.org/](https://doi.org/10.1016/j.epsl.2015.10.053)
 1055 [10.1016/j.epsl.2015.10.053](https://doi.org/10.1016/j.epsl.2015.10.053) doi: 10.1016/j.epsl.2015.10.053
- 1056 Jones, D. (2020). *East african rift temperature and heat flow model (earth)*. British
 1057 Geological Survey. Retrieved from [https://www.bgs.ac.uk/services/ngdc/](https://www.bgs.ac.uk/services/ngdc/citedData/catalogue/e1bc2841-81c2-4b6e-ae5b-301f3bf82b68.html)
 1058 [citedData/catalogue/e1bc2841-81c2-4b6e-ae5b-301f3bf82b68.html](https://www.bgs.ac.uk/services/ngdc/citedData/catalogue/e1bc2841-81c2-4b6e-ae5b-301f3bf82b68.html) doi:
 1059 [10.5285/E1BC2841-81C2-4B6E-AE5B-301F3BF82B68](https://doi.org/10.5285/E1BC2841-81C2-4B6E-AE5B-301F3BF82B68)
- 1060 Kaislaniemi, L., & van Hunen, J. (2014). Dynamics of lithospheric thinning and
 1061 mantle melting by edge-driven convection: Application to Moroccan Atlas
 1062 mountains. *Geochem. Geophys. Geosyst.*, *15*(8), 3175–3189. Retrieved from
 1063 <https://doi.org/10.1002/2014gc005414> doi: 10.1002/2014gc005414
- 1064 Katsura, T., & Ito, E. (1989). The system Mg_2SiO_4 - Fe_2SiO_4 at high pressures
 1065 and temperatures: Precise determination of stabilities of olivine, modi-
 1066 fied spinel, and spinel. *J. Geophys. Res. Solid Earth*, *94*(B11), 15663–
 1067 15670. Retrieved from <https://doi.org/10.1029/jb094ib11p15663> doi:
 1068 [10.1029/jb094ib11p15663](https://doi.org/10.1029/jb094ib11p15663)
- 1069 Keir, D., Doubre, C., & Leroy, S. (2017). *Afar margin northern profile*. Interna-
 1070 tional Federation of Digital Seismograph Networks. Retrieved from [https://](https://www.fdsn.org/networks/detail/YQ_2017/)
 1071 www.fdsn.org/networks/detail/YQ_2017/ doi: 10.7914/SN/YQ_2017
- 1072 Keir, D., & Hammond, J. O. (2009). *Afar0911*. International Federation of Digi-
 1073 tal Seismograph Networks. Retrieved from [https://www.fdsn.org/networks/](https://www.fdsn.org/networks/detail/2H_2009/)
 1074 [detail/2H_2009/](https://www.fdsn.org/networks/detail/2H_2009/) doi: 10.7914/SN/2H_2009
- 1075 Kemp, M., Jenkins, J., Maclennan, J., & Cottaar, S. (2019). X-discontinuity and
 1076 transition zone structure beneath Hawaii suggests a heterogeneous plume.
 1077 *Earth Planet. Sci. Lett.*, *527*, 115781. Retrieved from [https://doi.org/](https://doi.org/10.1016/j.epsl.2019.115781)
 1078 [10.1016/j.epsl.2019.115781](https://doi.org/10.1016/j.epsl.2019.115781) doi: 10.1016/j.epsl.2019.115781
- 1079 Keranen, K. (2013). *Exploring extensional tectonics beyond the Ethiopian*
 1080 *Rift*. International Federation of Digital Seismograph Networks. Re-
 1081 trieved from https://www.fdsn.org/networks/detail/YY_2013/ doi:
 1082 [10.7914/SN/YY_2013](https://doi.org/10.7914/SN/YY_2013)
- 1083 Kind, R. (1998). *Namibia*. GFZ Data Services. Retrieved from [https://geofon.gfz](https://geofon.gfz-potsdam.de/doi/network/XC/1998)
 1084 [-potsdam.de/doi/network/XC/1998](https://geofon.gfz-potsdam.de/doi/network/XC/1998) doi: 10.14470/KP6443475642
- 1085 King, S. D., & Anderson, D. L. (1998). Edge-driven convection. *Earth Planet.*

- 1086 *Sci. Lett.*, 160(3-4), 289–296. Retrieved from [https://doi.org/10.1016/s0012-821x\(98\)00089-2](https://doi.org/10.1016/s0012-821x(98)00089-2) doi: 10.1016/s0012-821x(98)00089-2
- 1087
- 1088 King, S. D., & Ritsema, J. (2000). African hot spot volcanism: Small-scale con-
1089 vection in the upper mantle beneath cratons. *Science*, 290(5494), 1137–1140.
1090 Retrieved from <https://doi.org/10.1126/science.290.5494.1137> doi: 10
1091 .1126/science.290.5494.1137
- 1092 Kounoudis, R., Bastow, I. D., Ebinger, C. J., Ogden, C. S., Ayele, A., Bendick, R.,
1093 ... Kibret, B. (2021). Body-Wave Tomographic Imaging of the Turkana
1094 Depression: Implications for Rift Development and Plume-Lithosphere Interac-
1095 tions. *Geochem. Geophys. Geosyst.*, 22(8). doi: 10.1029/2021gc009782
- 1096 Lange, D., & Soler, V. (2019). *Monitoring the unrest of elhierro island with seis-*
1097 *mic observations*. GFZ Data Services. Retrieved from [https://geofon.gfz](https://geofon.gfz-potsdam.de/doi/network/2L/2015)
1098 [-potsdam.de/doi/network/2L/2015](https://geofon.gfz-potsdam.de/doi/network/2L/2015) doi: 10.14470/7Y7560573304
- 1099 Langston, C. A. (1979). Structure under Mount Rainier, Washington, in-
1100 ferred from teleseismic body waves. *J. Geophys. Res. Solid Earth*, 84(B9),
1101 4749. Retrieved from <https://doi.org/10.1029/jb084ib09p04749> doi:
1102 10.1029/jb084ib09p04749
- 1103 Lee, D.-C., Halliday, A. N., Fitton, J., & Poli, G. (1994). Isotopic variations
1104 with distance and time in the volcanic islands of the Cameroon line: evi-
1105 dence for a mantle plume origin. *Earth Planet. Sci. Lett.*, 123(1-3), 119–138.
1106 Retrieved from [https://doi.org/10.1016/0012-821x\(94\)90262-3](https://doi.org/10.1016/0012-821x(94)90262-3) doi:
1107 10.1016/0012-821x(94)90262-3
- 1108 Lekic, V., Cottaar, S., Dziewonski, A., & Romanowicz, B. (2012). Cluster anal-
1109 ysis of global lower mantle tomography: A new class of structure and im-
1110 plications for chemical heterogeneity. *Earth Planet. Sci. Lett.*, 357, 68–77.
1111 Retrieved from <https://doi.org/10.1016/j.epsl.2012.09.014> doi:
1112 10.1016/j.epsl.2012.09.014
- 1113 Leroy, S., Keir, D., & Stuart, G. (2009). *Young conjugate margins lab in the Gulf*
1114 *of Aden*. International Federation of Digital Seismograph Networks. Retrieved
1115 from https://www.fdsn.org/networks/detail/XW_2009/ doi: 10.7914/SN/
1116 XW_2009
- 1117 Levander, A., Humphreys, G., & Ryan, P. (2009). *Program to investigate convec-*
1118 *tive Alboran Sea system overturn*. International Federation of Digital Seismo-

- 1119 graph Networks. Retrieved from [https://www.fdsn.org/networks/detail/](https://www.fdsn.org/networks/detail/XB_2009/)
 1120 XB_2009/ doi: 10.7914/SN/XB.2009
- 1121 Levèque, J.-J., & RESIF. (2010). *Horn of Africa (Ethiopia, Yemen) broad-band*
 1122 *experiment (Horn of Africa, RESIF-SISMOB)*. RESIF - Réseau Sismologique
 1123 et géodésique Français. Retrieved from [https://seismology.resif.fr/](https://seismology.resif.fr/networks/#/YR_1999)
 1124 networks/#/YR_1999 doi: 10.15778/RESIF.YR1999
- 1125 Liégeois, J.-P., Benhallou, A., Azzouni-Sekkal, A., Yahiaoui, R., & Bonin, B.
 1126 (2005). The Hoggar swell and volcanism: Reactivation of the Precambrian
 1127 Tuareg shield during Alpine convergence and West African Cenozoic vol-
 1128 canism. In *Plates, plumes and paradigms*. Geological Society of Amer-
 1129 ica. Retrieved from <https://doi.org/10.1130/0-8137-2388-4.379> doi:
 1130 10.1130/0-8137-2388-4.379
- 1131 Ligorria, J. P., & Ammon, C. J. (1999). Iterative deconvolution and receiver-
 1132 function estimation. *Bull. Seis. Soc. Am.*, *89*(5), 1395–1400. Retrieved from
 1133 <https://doi.org/10.1785/BSSA0890051395> doi: 10.1785/BSSA0890051395
- 1134 Lithgow-Bertelloni, C., & Silver, P. G. (1998). Dynamic topography, plate driving
 1135 forces and the African superswell. *Nature*, *395*(6699), 269–272. Retrieved from
 1136 <https://doi.org/10.1038/26212> doi: 10.1038/26212
- 1137 Lustrino, M., & Wilson, M. (2007). The circum-Mediterranean anorogenic Ceno-
 1138 zoic igneous province. *Earth Sci. Rev.*, *81*(1-2), 1–65. Retrieved from [https://](https://doi.org/10.1016/j.earscirev.2006.09.002)
 1139 doi.org/10.1016/j.earscirev.2006.09.002 doi: 10.1016/j.earscirev.2006
 1140 .09.002
- 1141 Marignier, A., Ferreira, A. M. G., & Kitching, T. (2020). The probability of
 1142 mantle plumes in global tomographic models. *Geochem. Geophys. Geosyst.*,
 1143 *21*(9). Retrieved from <https://doi.org/10.1029/2020gc009276> doi:
 1144 10.1029/2020gc009276
- 1145 Matthews, S., Shorttle, O., & Maclennan, J. (2016). The temperature of the ice-
 1146 landic mantle from olivine-spinel aluminum exchange thermometry. *Geochem.*
 1147 *Geophys. Geosyst.*, *17*(11), 4725–4752. Retrieved from [https://doi.org/10](https://doi.org/10.1002/2016gc006497)
 1148 [.1002/2016gc006497](https://doi.org/10.1002/2016gc006497) doi: 10.1002/2016gc006497
- 1149 MedNet Project Partner Institutions. (1988). *Mediterranean Very Broadband Seis-*
 1150 *mographic Network (MedNet)*. Istituto Nazionale di Geofisica e Vulcanologia
 1151 (INGV). Retrieved from <http://cnt.rm.ingv.it/instruments/network/MN>

- 1152 doi: 10.13127/SD/FBBBTDTD6Q
- 1153 Megies, T., Beyreuther, M., Barsch, R., Krischer, L., & Wassermann, J. (2011).
 1154 ObsPy – What can it do for data centers and observatories? *Astron. Geo-*
 1155 *phys.*, 54(1). Retrieved from <http://doi.org/10.4401/ag-4838> doi:
 1156 10.4401/ag-4838
- 1157 Melluso, L., Cucciniello, C., le Roex, A., & Morra, V. (2016). The geochemistry
 1158 of primitive volcanic rocks of the Ankaratra volcanic complex, and source en-
 1159 richment processes in the genesis of the Cenozoic magmatism in Madagascar.
 1160 *Geochim. Cosmochim. Acta.*, 185, 435–452. Retrieved from [https://doi.org/](https://doi.org/10.1016/j.gca.2016.04.005)
 1161 [10.1016/j.gca.2016.04.005](https://doi.org/10.1016/j.gca.2016.04.005) doi: 10.1016/j.gca.2016.04.005
- 1162 Mériaux, C., Duarte, J., Duarte, S., Schellart, W., Chen, Z., Rosas, F., . . . Ter-
 1163 rinha, P. (2015). Capture of the Canary mantle plume material by the
 1164 Gibraltar arc mantle wedge during slab rollback. *Geophys. J. Int.*, 201(3),
 1165 1717–1721. Retrieved from <https://doi.org/10.1093/gji/ggv120> doi:
 1166 10.1093/gji/ggv120
- 1167 Michon, L. (2015). The volcanism of the Comoros Archipelago integrated at a re-
 1168 gional scale. In *Active volcanoes of the southwest indian ocean* (pp. 333–344).
 1169 Springer Berlin Heidelberg. Retrieved from [https://doi.org/10.1007/978-3-](https://doi.org/10.1007/978-3-642-31395-0_21)
 1170 [642-31395-0_21](https://doi.org/10.1007/978-3-642-31395-0_21) doi: 10.1007/978-3-642-31395-0_21
- 1171 Milelli, L., Fourel, L., & Jaupart, C. (2012). A lithospheric instability origin for
 1172 the Cameroon Volcanic Line. *Earth Planet. Sci. Lett.*, 335–336, 80–87. Re-
 1173 trieved from <https://doi.org/10.1016/j.epsl.2012.04.028> doi: 10.1016/
 1174 [j.epsl.2012.04.028](https://doi.org/10.1016/j.epsl.2012.04.028)
- 1175 Miller, M. S., O'Driscoll, L. J., Butcher, A. J., & Thomas, C. (2015). Imaging
 1176 Canary Island hotspot material beneath the lithosphere of Morocco and south-
 1177 ern Spain. *Earth Planet. Sci. Lett.*, 431, 186–194. Retrieved from [https://](https://doi.org/10.1016/j.epsl.2015.09.026)
 1178 doi.org/10.1016/j.epsl.2015.09.026 doi: 10.1016/j.epsl.2015.09.026
- 1179 Missenard, Y., & Cadoux, A. (2011). Can Moroccan Atlas lithospheric thinning
 1180 and volcanism be induced by edge-driven convection? *Terra Nova*, 24(1), 27–
 1181 33. Retrieved from <https://doi.org/10.1111/j.1365-3121.2011.01033.x>
 1182 doi: 10.1111/j.1365-3121.2011.01033.x
- 1183 Monaco, M., Dannberg, J., Gasmöller, R., & Pugh, S. (2022). The segregation
 1184 of recycled basaltic material within mantle plumes explains the detection of

- 1185 the x-discontinuity beneath hotspots: 2d geodynamic simulations. *Earth and*
 1186 *Space Science Open Archive*, 25. Retrieved from [https://doi.org/10.1002/](https://doi.org/10.1002/essoar.10512065.1)
 1187 [essoar.10512065.1](https://doi.org/10.1002/essoar.10512065.1) doi: 10.1002/essoar.10512065.1
- 1188 Montigny, R., Ngounouno, I., & D eruelle, B. (2004).  ges KAr des roches
 1189 magmatiques du foss  de garoua (cameroun) : leur place dans le cadre
 1190 de la « ligne du cameroun ». *C. R. Geosci.*, 336(16), 1463–1471. Re-
 1191 trieved from <https://doi.org/10.1016/j.crte.2004.08.005> doi:
 1192 10.1016/j.crte.2004.08.005
- 1193 Muirhead, J. D., Fischer, T. P., Oliva, S. J., Laizer, A., van Wijk, J., Currie,
 1194 C. A., ... Ebinger, C. J. (2020). Displaced cratonic mantle concen-
 1195 trates deep carbon during continental rifting. *Nature*, 582(7810), 67–72.
 1196 Retrieved from <https://doi.org/10.1038/s41586-020-2328-3> doi:
 1197 10.1038/s41586-020-2328-3
- 1198 Mulibo, G. D., & Nyblade, A. A. A. (2016). The seismotectonics of Southeastern
 1199 Tanzania: Implications for the propagation of the eastern branch of the East
 1200 African Rift. *Tectonophysics*, 674, 20–30. Retrieved from [https://doi.org/](https://doi.org/10.1016/j.tecto.2016.02.009)
 1201 [10.1016/j.tecto.2016.02.009](https://doi.org/10.1016/j.tecto.2016.02.009) doi: 10.1016/j.tecto.2016.02.009
- 1202 Nyblade, A. A. (2000). *Seismic investigation of deep structure beneath the Ethiopian*
 1203 *Plateau and Afar Depression*. International Federation of Digital Seismo-
 1204 graph Networks. Retrieved from [https://www.fdsn.org/networks/detail/](https://www.fdsn.org/networks/detail/XI_2000/)
 1205 [XI_2000/](https://www.fdsn.org/networks/detail/XI_2000/) doi: 10.7914/SN/XI_2000
- 1206 Nyblade, A. A. (2007). *Africa Array - Uganda/Tanzania*. International Fed-
 1207 eration of Digital Seismograph Networks. Retrieved from [https://www.fdsn](https://www.fdsn.org/networks/detail/ZP_2007/)
 1208 [.org/networks/detail/ZP_2007/](https://www.fdsn.org/networks/detail/ZP_2007/) doi: 10.7914/SN/ZP_2007
- 1209 Nyblade, A. A. (2010). *AfricaArray SE Tanzania Basin Experiment*. Interna-
 1210 tional Federation of Digital Seismograph Networks. Retrieved from [https://](https://www.fdsn.org/networks/detail/YH_2010/)
 1211 www.fdsn.org/networks/detail/YH_2010/ doi: 10.7914/SN/YH_2010
- 1212 Nyblade, A. A. (2015a). *AfricaArray - Namibia*. IRIS. Retrieved from [https://www](https://www.fdsn.org/networks/detail/8A_2015/)
 1213 [.fdsn.org/networks/detail/8A_2015/](https://www.fdsn.org/networks/detail/8A_2015/) doi: 10.7914/SN/8A_2015
- 1214 Nyblade, A. A. (2015b). *REU: Imaging the Bushveld Complex, South Africa*.
 1215 International Federation of Digital Seismograph Networks. Retrieved from
 1216 https://www.fdsn.org/networks/detail/ZT_2015/ doi: 10.7914/SN/
 1217 [ZT_2015](https://www.fdsn.org/networks/detail/ZT_2015/)

- 1218 Nyblade, A. A. (2017). *Broadband seismic experiment in NE Uganda to investigate*
 1219 *plume-lithosphere interactions*. International Federation of Digital Seismograph
 1220 Networks. Retrieved from https://www.fdsn.org/networks/detail/XW_2017
 1221 doi: 10.7914/SN/XW_2017
- 1222 Observatoire Volcanologique Du Piton De La Fournaise (OVPF), & Institut De
 1223 Physique Du Globe De Paris (IPGP). (2008). *Seismic, tiltmeter, extensometer,*
 1224 *magnetic and weather permanent networks on Piton de la Fournaise volcano*
 1225 *and La Réunion*. Institut de physique du globe de Paris (IPGP), Université de
 1226 Paris. Retrieved from <http://volobsis.ipgp.fr/networks/detail/PF> doi:
 1227 10.18715/REUNION.PF
- 1228 O'Connor, J. M., Jokat, W., Regelous, M., Kuiper, K. F., Miggins, D. P., & Kop-
 1229 pers, A. A. P. (2019). Superplume mantle tracked isotopically the length
 1230 of Africa from the Indian Ocean to the Red Sea. *Nat. Commun.*, 10(1).
 1231 Retrieved from <https://doi.org/10.1038/s41467-019-13181-7> doi:
 1232 10.1038/s41467-019-13181-7
- 1233 Owens, T. J., & Nyblade, A. A. (1994). *Seismic investigations of the lithospheric*
 1234 *structure of the Tanzanian Craton*. International Federation of Digital Seismo-
 1235 graph Networks. Retrieved from [https://www.fdsn.org/networks/detail/](https://www.fdsn.org/networks/detail/XD_1994/)
 1236 [XD_1994/](https://www.fdsn.org/networks/detail/XD_1994/) doi: 10.7914/SN/XD_1994
- 1237 Owens, T. J., Nyblade, A. A., Gurrola, H., & Langston, C. A. (2000). Mantle transi-
 1238 tion zone structure beneath Tanzania, East Africa. *Geophys. Res. Lett.*, 27(6),
 1239 827–830. Retrieved from <https://doi.org/10.1029/1999GL005429> doi: 10
 1240 .1029/1999GL005429
- 1241 Penn State University. (2004). *AfricaArray*. International Federation of Digi-
 1242 tal Seismograph Networks. Retrieved from [https://www.fdsn.org/networks/](https://www.fdsn.org/networks/detail/AF/)
 1243 [detail/AF/](https://www.fdsn.org/networks/detail/AF/) doi: 10.7914/SN/AF
- 1244 Pik, R., Marty, B., & Hilton, D. (2006). How many mantle plumes in Africa? The
 1245 geochemical point of view. *Chem. Geol.*, 226(3-4), 100–114. Retrieved from
 1246 <https://doi.org/10.1016/j.chemgeo.2005.09.016> doi: 10.1016/j.chemgeo
 1247 .2005.09.016
- 1248 Priestley, K., McKenzie, D., Debayle, E., & Pilidou, S. (2008). The African upper
 1249 mantle and its relationship to tectonics and surface geology. *Geophys. J. Int.*,
 1250 175(3), 1108–1126. Retrieved from <https://doi.org/10.1111/j.1365-246x>

- 1251 .2008.03951.x doi: 10.1111/j.1365-246x.2008.03951.x
- 1252 Priestley, K., McKenzie, D., & Ho, T. (2018). A lithosphere–asthenosphere bound-
 1253 ary—A global model derived from multimode surface-wave tomography and
 1254 petrology. *Lithospheric discontinuities*, 111–123. Retrieved from [https://](https://doi.org/10.1002/9781119249740.ch6)
 1255 doi.org/10.1002/9781119249740.ch6 doi: 10.1002/9781119249740.ch6
- 1256 Pugh, S., Jenkins, J., Boyce, A., & Cottaar, S. (2021). Global receiver function
 1257 observations of the X-discontinuity reveal recycled basalt beneath hotspots.
 1258 *Earth Planet. Sci. Lett.*, 561, 116813. Retrieved from [https://doi.org/](https://doi.org/10.1016/j.epsl.2021.116813)
 1259 [10.1016/j.epsl.2021.116813](https://doi.org/10.1016/j.epsl.2021.116813) doi: 10.1016/j.epsl.2021.116813
- 1260 Rakhmanov, E. A., Saff, E. B., & Zhou, Y. (1994). Minimal discrete energy on the
 1261 sphere. *Math. Res. Lett.*, 1(6), 647–662. Retrieved from [https://dx.doi.org/](https://dx.doi.org/10.4310/MRL.1994.v1.n6.a3)
 1262 [10.4310/MRL.1994.v1.n6.a3](https://dx.doi.org/10.4310/MRL.1994.v1.n6.a3) doi: 10.4310/MRL.1994.v1.n6.a3
- 1263 Reed, C., Gao, S., Liu, K., & Yu, Y. (2016). The mantle transition zone be-
 1264 neath the Afar Depression and adjacent regions: implications for mantle
 1265 plumes and hydration. *Geophys. J. Int.*, 205(3), 1756–1766. Retrieved from
 1266 <https://doi.org/10.1093/gji/ggw116> doi: 10.1093/gji/ggw116
- 1267 Rein, T., Hannemann, K., Thomas, C., & Korn, M. (2020). Location and char-
 1268 acteristics of the X-discontinuity beneath SW Morocco and the adjacent
 1269 shelf area using P-wave receiver functions. *Geophys. J. Int.*, 223(3), 1780–
 1270 1793. Retrieved from <https://doi.org/10.1093/gji/ggaa379> doi:
 1271 [10.1093/gji/ggaa379](https://doi.org/10.1093/gji/ggaa379)
- 1272 Reusch, A. M., Nyblade, A. A., Tibi, R., Wiens, D. A., Shore, P. J., Bekoa, A., ...
 1273 Nnange, J. M. (2011). Mantle transition zone thickness beneath Cameroon:
 1274 evidence for an upper mantle origin for the Cameroon Volcanic Line. *Geo-*
 1275 *phys. J. Int.*, 187(3), 1146–1150. Retrieved from [https://doi.org/10.1111/](https://doi.org/10.1111/j.1365-246x.2011.05239.x)
 1276 [j.1365-246x.2011.05239.x](https://doi.org/10.1111/j.1365-246x.2011.05239.x) doi: 10.1111/j.1365-246x.2011.05239.x
- 1277 Reusch, A. M., Nyblade, A. A., Wiens, D. A., Shore, P. J., Ateba, B., Tabod,
 1278 C. T., & Nnange, J. M. (2010). Upper mantle structure beneath Cameroon
 1279 from body wave tomography and the origin of the Cameroon Volcanic
 1280 Line. *Geochem. Geophys. Geosyst.*, 11(10), n/a–n/a. Retrieved from
 1281 <https://doi.org/10.1029/2010gc003200> doi: 10.1029/2010gc003200
- 1282 Revenaugh, J., & Jordan, T. H. (1991). Mantle layering from ScS reverberations: 3.
 1283 the upper mantle. *J. Geophys. Res. Solid Earth*, 96(B12), 19781–19810. Re-

- 1284 trieved from <https://doi.org/10.1029/91jb01487> doi: 10.1029/91jb01487
- 1285 Ritsema, J., Deuss, A., van Heijst, H. J., & Woodhouse, J. H. (2010). S40rts: a
1286 degree-40 shear-velocity model for the mantle from new Rayleigh wave disper-
1287 sion, teleseismic traveltimes and normal-mode splitting function measurements.
1288 *Geophys. J. Int.*, *184*(3), 1223–1236. Retrieved from [https://doi.org/](https://doi.org/10.1111/j.1365-246x.2010.04884.x)
1289 10.1111/j.1365-246x.2010.04884.x doi: 10.1111/j.1365-246x.2010.04884.x
- 1290 Ritsema, J., van Heijst, H., & Woodhouse, J. (1999). Complex shear wave velocity
1291 structure imaged beneath Africa and Iceland. *Science*, *286*, 1925–1928.
- 1292 Roberts, E. M., Stevens, N. J., O'Connor, P. M., Dirks, P. H. G. M., Gottfried,
1293 M. D., Clyde, W. C., . . . Hemming, S. (2012). Initiation of the western
1294 branch of the East African Rift coeval with the eastern branch. *Nat. Geosci.*,
1295 *5*(4), 289–294. Retrieved from <https://doi.org/10.1038/ngeo1432> doi:
1296 10.1038/ngeo1432
- 1297 Rooney, T. O. (2017). The Cenozoic magmatism of East-Africa: Part I–
1298 Flood basalts and pulsed magmatism. *Lithos*, *286–287*, 264–301. Re-
1299 trieved from <https://doi.org/10.1016/j.lithos.2017.05.014> doi:
1300 10.1016/j.lithos.2017.05.014
- 1301 Rooney, T. O., Herzberg, C., & Bastow, I. D. (2012). Elevated mantle tempera-
1302 ture beneath East Africa. *Geology*, *40*(1), 27–30. Retrieved from [https://doi](https://doi.org/10.1130/g32382.1)
1303 .org/10.1130/g32382.1 doi: 10.1130/g32382.1
- 1304 Saki, M., Thomas, C., Nippres, S. E., & Lessing, S. (2015). Topography of up-
1305 per mantle seismic discontinuities beneath the North Atlantic: The Azores,
1306 Canary and Cape Verde plumes. *Earth Planet. Sci. Lett.*, *409*, 193–202.
1307 Retrieved from <https://doi.org/10.1016/j.epsl.2014.10.052> doi:
1308 10.1016/j.epsl.2014.10.052
- 1309 San Fernando Royal Naval Observatory (ROA), Universidad Complutense De
1310 Madrid (UCM), Helmholtz-Zentrum Potsdam Deutsches GeoForschungsZen-
1311 trum (GFZ), Universidade De Evora (UEVORA, Portugal), & Institute Scien-
1312 tificque Of RABAT (ISRABAT, Morocco). (1996). *The Western Mediterranean*
1313 *BB seismic Network*. Deutsches GeoForschungsZentrum GFZ. Retrieved from
1314 <http://geofon.gfz-potsdam.de/doi/network/WM> doi: 10.14470/JZ581150
- 1315 Schaeffer, A. J., & Lebedev, S. (2013). Global shear speed structure of the upper
1316 mantle and transition zone. *Geophys. J. Int.*, *194*(1), 417–449. Retrieved from

- 1317 <https://doi.org/10.1093/gji/ggt095> doi: 10.1093/gji/ggt095
- 1318 Schaeffer, A. J., & Lebedev, S. (2014). Imaging the North American continent using
 1319 waveform inversion of global and USArray data. *Earth Planet. Sci. Lett.*, *402*,
 1320 26–41. Retrieved from <https://doi.org/10.1016/j.epsl.2014.05.014> doi:
 1321 10.1016/j.epsl.2014.05.014
- 1322 Schmerr, N. (2015). Imaging mantle heterogeneity with upper mantle seismic dis-
 1323 continuities. In *The earth's heterogeneous mantle* (pp. 79–104). Springer In-
 1324 ternational Publishing. Retrieved from https://doi.org/10.1007/978-3-319-15627-9_3
 1325 -15627-9_3 doi: 10.1007/978-3-319-15627-9_3
- 1326 Schmerr, N., Kelly, B. M., & Thorne, M. S. (2013). Broadband array observations
 1327 of the 300 km seismic discontinuity. *Geophys. Res. Lett.*, *40*(5), 841–846. Re-
 1328 trieved from <https://doi.org/10.1002/grl.50257> doi: 10.1002/grl.50257
- 1329 Scripps Institution of Oceanography. (1986). *Global Seismograph Network -*
 1330 *IRIS/IDA*. International Federation of Digital Seismograph Networks.
 1331 Retrieved from <https://www.fdsn.org/networks/detail/II/> doi:
 1332 10.7914/SN/II
- 1333 Silver, P. (1997). *Anatomy of an Archean Craton, South Africa, A Multidisciplinary*
 1334 *Experiment across the Kaapvaal Craton*. International Federation of Digital
 1335 Seismograph Networks. Retrieved from [https://www.fdsn.org/networks/](https://www.fdsn.org/networks/detail/XA_1997/)
 1336 [detail/XA_1997/](https://www.fdsn.org/networks/detail/XA_1997/) doi: 10.7914/SN/XA_1997
- 1337 Simmons, N. A., Forte, A. M., & Grand, S. P. (2007). Thermochemical structure
 1338 and dynamics of the African superplume. *Geophys. Res. Lett.*, *34*(2). Retrieved
 1339 from <https://doi.org/10.1029/2006gl028009> doi: 10.1029/2006gl028009
- 1340 Sodoudi, F., Yuan, X., Kind, R., Lebedev, S., Adam, J. M.-C., Kästle, E., &
 1341 Tilmann, F. (2013). Seismic evidence for stratification in composi-
 1342 tion and anisotropic fabric within the thick lithosphere of kalahari cra-
 1343 ton. *Geochem. Geophys. Geosyst.*, *14*(12), 5393–5412. Retrieved from
 1344 <https://doi.org/10.1002/2013gc004955> doi: 10.1002/2013gc004955
- 1345 Tepp, G., Ebinger, C. J., Zal, H., Gallacher, R., Accardo, N., Shillington, D. J.,
 1346 ... Kamihanda, G. (2018). Seismic anisotropy of the upper mantle below
 1347 the western rift, east africa. *J. Geophys. Res. Solid Earth*, *123*(7), 5644–
 1348 5660. Retrieved from <https://doi.org/10.1029/2017jb015409> doi:
 1349 10.1029/2017jb015409

- 1350 The ARGOS Project. (2012). *ARGOS - Alutu and regional geophysical observation*
 1351 *study*. International Federation of Digital Seismograph Networks. Retrieved
 1352 from https://www.fdsn.org/networks/detail/XM_2012/ doi: 10.7914/SN/
 1353 XM_2012
- 1354 Thirlwall, M. (1997). Pb isotopic and elemental evidence for OIB deriva-
 1355 tion from young HIMU mantle. *Chem. Geol.*, *139*(1-4), 51–74. Re-
 1356 trieved from [https://doi.org/10.1016/s0009-2541\(97\)00033-8](https://doi.org/10.1016/s0009-2541(97)00033-8) doi:
 1357 10.1016/s0009-2541(97)00033-8
- 1358 Thomas, C. (2010). *Morocco-muenster*. International Federation of Digital Seismo-
 1359 graph Networks. Retrieved from [https://www.fdsn.org/networks/detail/
 1360 3D_2010/](https://www.fdsn.org/networks/detail/3D_2010/) doi: 10.7914/SN/3D.2010
- 1361 Thompson, D. A., Hammond, J. O. S., Kendall, J.-M., Stuart, G. W., Helffrich,
 1362 G. R., Keir, D., ... Goitom, B. (2015). Hydrous upwelling across the mantle
 1363 transition zone beneath the Afar Triple Junction. *Geochem. Geophys. Geosyst.*,
 1364 *16*(3), 834–846. Retrieved from <https://doi.org/10.1002/2014gc005648>
 1365 doi: 10.1002/2014gc005648
- 1366 Thompson, D. A., Helffrich, G., Bastow, I., Kendall, J.-M., Wookey, J., Eaton,
 1367 D., & Snyder, D. (2011). Implications of a simple mantle transition zone
 1368 beneath cratonic North America. *Earth Planet. Sci. Lett.*, *312*(1-2), 28–
 1369 36. Retrieved from <https://doi.org/10.1016/j.epsl.2011.09.037> doi:
 1370 10.1016/j.epsl.2011.09.037
- 1371 Tilmann, F., Yuan, X., Rumpker, G., & Rindraharisaona, E. (2012). *SELA-*
 1372 *SOMA Project, Madagascar 2012-2014*. GFZ Data Services. Retrieved
 1373 from <http://geofon.gfz-potsdam.de/doi/network/ZE/2012> doi:
 1374 10.14470/MR7567431421
- 1375 Tsekhmistrenko, M., Sigloch, K., Hosseini, K., & Barruol, G. (2021). A tree of Indo-
 1376 African mantle plumes imaged by seismic tomography. *Nat. Geosci.*, *14*(8),
 1377 612–619. Retrieved from <https://doi.org/10.1038/s41561-021-00762-9>
 1378 doi: 10.1038/s41561-021-00762-9
- 1379 Utrecht University (UU Netherlands). (1983). *NARS*. International Federation
 1380 of Digital Seismograph Networks. Retrieved from [https://www.fdsn.org/
 1381 networks/detail/NR/](https://www.fdsn.org/networks/detail/NR/) doi: 10.7914/SN/NR
- 1382 van den Bogaard, P. (2013). The origin of the Canary Island Seamount Province -

- 1383 New ages of old seamounts. *Sci. Rep.*, 3(1). Retrieved from [https://doi.org/](https://doi.org/10.1038/srep02107)
 1384 10.1038/srep02107 doi: 10.1038/srep02107
- 1385 van der Lee, S., Deschamps, A., Margheriti, L., & Giardini, D. (1999). *Midsea -*
 1386 *mantle investigation of the deep suture between Eurasia and Africa.* Interna-
 1387 tional Federation of Digital Seismograph Networks. Retrieved from [https://](https://www.fdsn.org/networks/detail/YF.1999/)
 1388 www.fdsn.org/networks/detail/YF.1999/ doi: 10.7914/SN/YF_1999
- 1389 van Stiphout, A. M., Cottaar, S., & Deuss, A. (2019). Receiver function map-
 1390 ping of mantle transition zone discontinuities beneath Alaska using scaled 3-D
 1391 velocity corrections. *Geophys. J. Int.*, 219(2), 1432–1446. Retrieved from
 1392 <https://doi.org/10.1093/gji/ggz360> doi: 10.1093/gji/ggz360
- 1393 Velasco, A., Kaip, G., Wamalwa, A., & Patlan, E. (2011). *Seismic characteriza-*
 1394 *tion of menengai crater, kenya.* International Federation of Digital Seismo-
 1395 graph Networks. Retrieved from [https://www.fdsn.org/networks/detail/](https://www.fdsn.org/networks/detail/1C.2011/)
 1396 1C.2011/ doi: 10.7914/SN/1C_2011
- 1397 Vergne, J., Doubre, C., & Leroy, S. (2014). *Seismic network 7c:dora experiment*
 1398 *(resif-sismob).* RESIF - Réseau Sismologique et géodésique Français. Retrieved
 1399 from https://seismology.resif.fr/networks/#/7C_2009 doi: 10.15778/
 1400 RESIF.7C2009
- 1401 Weber, M., Silveira, G., & Schulze, A. (2007). *The COBO/CV-PLUME temporary*
 1402 *seismic network.* GFZ Data Services. Retrieved from [https://geofon.gfz](https://geofon.gfz-potsdam.de/doi/network/9A/2007)
 1403 [-potsdam.de/doi/network/9A/2007](https://geofon.gfz-potsdam.de/doi/network/9A/2007) doi: 10.14470/4N7552467332
- 1404 Widom, E., Hoernle, K. A., Shirey, S. B., & Schmincke, H.-U. (1999). Os isotope
 1405 systematics in the Canary Islands and Madeira: Lithospheric contamination
 1406 and mantle plume signatures. *J. Petrol.*, 40(2), 279–296. Retrieved from
 1407 <https://doi.org/10.1093/etroj/40.2.279> doi: 10.1093/etroj/40.2.279
- 1408 Wiens, D., & Nyblade, A. A. (2005). *Broadband Seismic Investigation of the*
 1409 *Cameroon Volcanic Line.* International Federation of Digital Seismograph Net-
 1410 works. Retrieved from <https://www.fdsn.org/networks/detail/XB.2005/>
 1411 doi: 10.7914/SN/XB.2005
- 1412 Williams, C. D., Mukhopadhyay, S., Rudolph, M. L., & Romanowicz, B. (2019).
 1413 Primitive helium is sourced from seismically slow regions in the lowermost
 1414 mantle. *Geochem. Geophys. Geosyst.*, 20(8), 4130–4145. Retrieved from
 1415 <https://doi.org/10.1029/2019gc008437> doi: 10.1029/2019gc008437

- 1416 Williams, Q., & Revenaugh, J. (2005). Ancient subduction, mantle eclogite, and the
 1417 300 km seismic discontinuity. *Geology*, *33*(1), 1. Retrieved from [https://doi](https://doi.org/10.1130/g20968.1)
 1418 [.org/10.1130/g20968.1](https://doi.org/10.1130/g20968.1) doi: 10.1130/g20968.1
- 1419 Wölbern, I., Rumpker, G., Link, K., & Sodoudi, F. (2012). Melt infiltration of
 1420 the lower lithosphere beneath the tanzania craton and the albertine rift
 1421 inferred from s receiver functions. *Geochem. Geophys. Geosyst.*, *13*(8),
 1422 n/a–n/a. Retrieved from <https://doi.org/10.1029/2012gc004167> doi:
 1423 10.1029/2012gc004167
- 1424 Woodland, A. B. (1998). The orthorhombic to high-*P* monoclinic phase transition in
 1425 Mg-Fe pyroxenes: Can it produce a seismic discontinuity? *Geophys. Res. Lett.*,
 1426 *25*(8), 1241–1244. Retrieved from <https://doi.org/10.1029/98gl00857> doi:
 1427 10.1029/98gl00857
- 1428 Wookey, J., Horleston, A., Leo, J. D., Thomas, C., Harnafi, M., & Elouai, D. (2011).
 1429 *CoMITAC Morocco-Bristol Network*. International Federation of Digital
 1430 Seismograph Networks. Retrieved from [https://www.fdsn.org/networks/](https://www.fdsn.org/networks/detail/ZI_2011/)
 1431 [detail/ZI_2011/](https://www.fdsn.org/networks/detail/ZI_2011/) doi: 10.7914/SN/ZI_2011
- 1432 Woolley, A. R., & Kjarsgaard, B. A. (2008). *Carbonatite occurrences of the world*.
 1433 Geological Survey of Canada.
- 1434 Wysession, M., Wiens, D., & Nyblade, A. A. (2011). *Investigation of sources of in-*
 1435 *traplate volcanism using passcal broadband instruments in Madagascar, the Co-*
 1436 *mores, and Mozambique*. International Federation of Digital Seismograph Net-
 1437 works. Retrieved from https://www.fdsn.org/networks/detail/XV_2011/
 1438 doi: 10.7914/SN/XV_2011
- 1439 Xu, F., Vidale, J. E., Earle, P. S., & Benz, H. M. (1998). Mantle discontinuities un-
 1440 der southern Africa from precursors to $P'P'_{df}$. *Geophys. Res. Lett.*, *25*(4), 571–
 1441 574. Retrieved from <https://doi.org/10.1029/98GL00122> doi: 10.1029/
 1442 98GL00122